Design, Optimization and Additive Manufacturing of Gradient Index Lenses for Scan Enhancement of Phased Array Antennas

MSc Thesis

Leonard Besse

Delft University of Technology

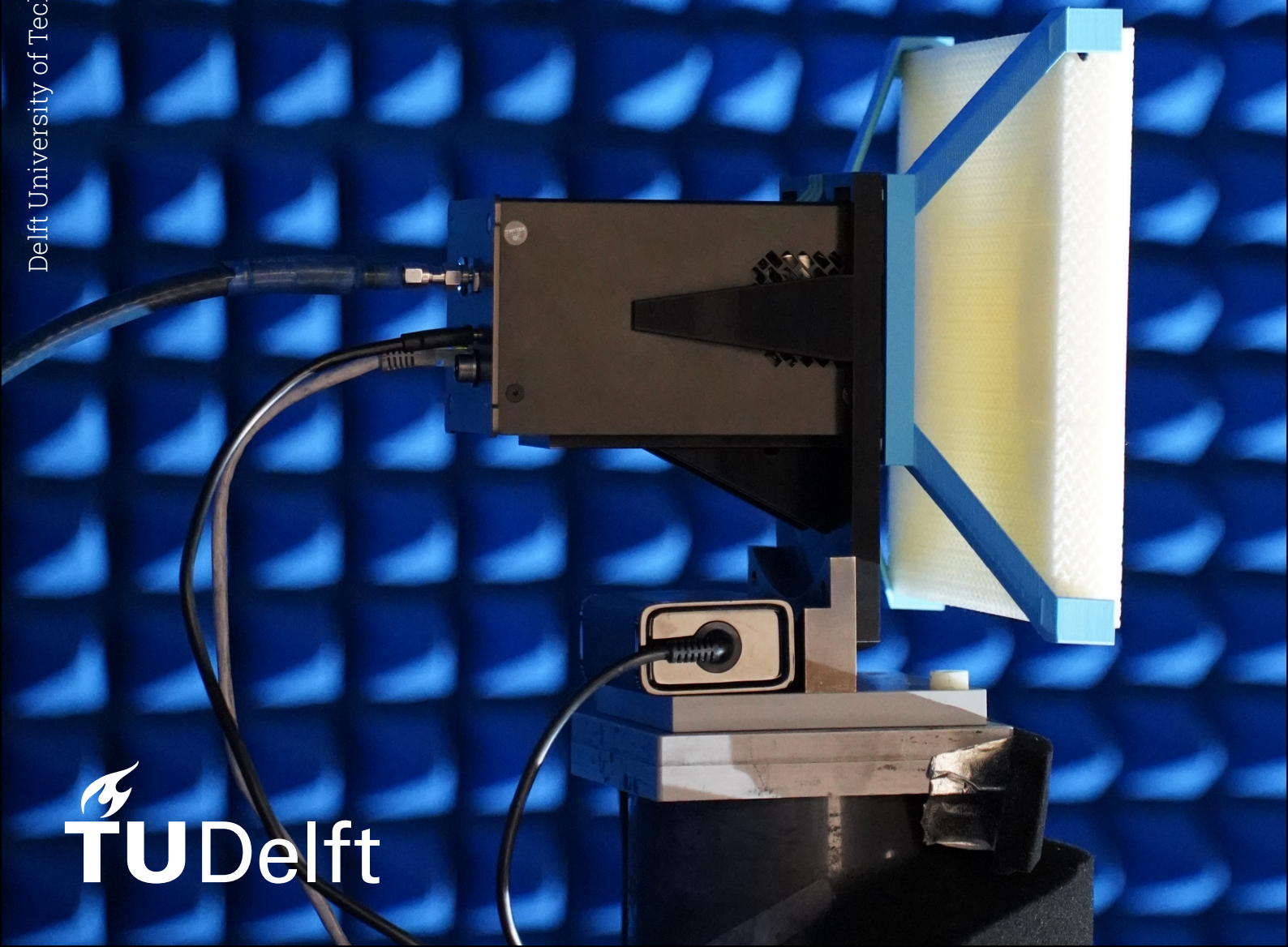

TU Delft

Design, Optimization and Additive Manufacturing of Gradient Index Lenses for Scan Enhancement of Phased Array Antennas

by

Leonard Besse

to obtain the degree of Master of Science

at the Delft University of Technology,

to be defended publicly on Thursday March 5, 2026 at 10:00 AM.

Student number:	4798864	
Project duration:	June 11, 2025 – March 05, 2026	
Supervision:	Prof. K. Masania,	Responsible Supervisor
	Dr. Y. Aslan,	Co-Supervisor
	Dr. S. Patranabish,	Daily Supervisor
Assessment committee:	Dr. I. Uriol Balbin,	Chair
	Prof. K. Masania,	Responsible Supervisor
	Dr. M. Alonso-delPino,	Independent Examiner

An electronic version of this thesis is available at `http://repository.tudelft.nl/`.

TU Delft

Preface

”Therefore, though I am but ill qualified for a pioneer, in the application of these two semi-sciences to the whale, I will do my endeavor. I try all things; I achieve what I can.”
-Herman Melville

This project is the result of a collaboration between the Shaping Matter Lab (SML) at the Faculty of Aerospace Engineering, and the Microwave Sensing, Signals and Systems group (MS3) at the Faculty of Electrical Engineering, Mathematics and Computer Sciences. After following courses on electromagnetics during my Masters programme, I discovered I had interest for electrical engineering and physics, and set out to find a topical thesis.

I first and foremost want to thank Prof. Kunal Masania, Yanki Aslan and Sourav Patranabish for their guidance and supervision, and enabling me to explore this topic close to my interests. I would also like to thank Pascal Aubry for his help with the antenna measurements found in this thesis, as well as Sina Hashemizadeh (IT’IS) for the dielectric spectroscopy measurements. Finally, I am thankful to the staff and students of SML and MS3, and my friends and family who have supported me through my studies and made of it an overall pleasant experience.

Leonard Besse
Delft, February 2026

Summary

Phased array antennas are a key element of our wireless communications infrastructure, enabling Multiple-Input Multiple-Output (MIMO) communication and sensing. However, there are some inherent challenges and limitations associated with phased array antennas; notably, the antenna gain typically decays as the beam is steered away from broadside, which imposes a limit on the usable scan range.

One promising approach to mitigate this effect is via dielectric lenses, which are becoming more practical as communication standards shift towards higher frequencies. Furthermore, advances in additive manufacturing enable the fabrication of lenses with a spatially varying refractive index, allowing for more freedom in the form factor compared to homogeneous lenses. Such Gradient Index (GRIN) lenses could offer a drop-in solution to mitigate scan loss in phased array antennas. However, the optimization of GRIN lenses remains challenging, and few methods have been presented to optimize arbitrarily varying GRIN profiles.

This thesis investigates the design, optimization, fabrication, and experimental validation of an additively manufactured flat GRIN lens to enhance the scan coverage of a TMYTEK BBox 5G $28\,\mathrm{GHz}$ phased array antenna, which has a scan range of approximately $\pm 45^{\circ}$.

GRIN media is realized using additively manufactured sub-wavelength dielectric crystals. Structures with an arbitrary spatial variation of density are synthesized using continuously graded Triply Periodic Minimal Surface (TPMS) structures. GRIN media is fabricated using Polylactic Acid (PLA) filament, of which the complex permittivity was measured with help from the IT'IS foundation.

A novel method is proposed to parametrize GRIN media, where the refractive index distribution of the lens is represented as a Fourier series expansion, normalized to the achievable limits of the refractive index set by the manufacturing constraints. This approach is well suited to curved-ray Geometrical Optics (GO), as the gradient of the refractive index can be computed analytically.

Using this parametrization, GRIN lenses are designed by optimizing for the Fourier coefficients. A fitness function is derived based on a model for the field at the aperture, allowing for optimization with a sparse distribution of GO rays. The fitness function is minimized using a Particle Swarm Optimization algorithm. This approach is validated by optimizing a Luneburg lens, demonstrating close agreement between the optimized and theoretical GRIN profiles.

This method is then applied to design a flat GRIN lens to enhance the scan coverage of a phased array antenna. The optimized lens is experimentally evaluated in the Delft University Chamber for Antenna Tests facility, increasing the scan coverage of the TMYTEK BBox phased array antenna by ± 10 degrees and demonstrating the possibility of drop-in improvements to the scan coverage of phased array antennas using GRIN lenses.

Acronyms

DRA Dielectric Resonator Antennas. 37

FDTD Finite Difference Time Domain. 17
FEM Finite Element Modelling. 17
FFF Fused Filament Fabrication. 9, 10, 13, 14, 26, 35, 36

GO Geometrical Optics. ii, 11, 17, 24, 30, 36, 37
GRIN Gradient Index. ii, vi, 2–11, 13, 19–24, 28–38, 43, 46, 50

LCP Liquid Crystal Polymer. 37

MIMO Multiple-Input Multiple-Output. ii
MoM Method of Moments. 17

ODE Ordinary Differential Equations. 8, 18, 19

PAFL Phased Array-Fed Lens. 7
PLA Polylactic Acid. ii, 15, 35, 37
PO Physical Optics. 7, 17, 37
PP Polypropylene. 14, 15
PSO Particle Swarm Optimization. ii, 8, 23, 24, 28, 30, 31

QCTO Quasi-Conformal Transformation Optics. 5

RCS Radar Cross-Section. 29, 30, 36

SVL Spatially Variant Lattice. 14, 35

TO Transformation Optics. 5
TPMS Triply Periodic Minimal Surface. ii, 11, 14, 35, 38

Nomenclature

$[T]$	Transformation matrix for the target direction, see equation (2.17)	[–]
δ_i	Volume fraction of inclusions	[–]
η	Impedance of free space	[Ω]
$\hat{n}$	Unit vector normal to the interface, see equation (2.6)	[m]
$\hat{s}$	Unit vector in the ray direction	[–]
$\hat{s}^i$	Unit vector of the transmitted ray, see equation (2.6)	[–]
$\hat{s}^t$	Unit vector of the incident ray, see equation (2.6)	[–]
λ_0	Wavelength in free space	[m]
$\mathbf{E}_{0,ap}$	Magnitude of the electric field at the aperture	[V/m]
$\mathbf{E}_{ap}$	Complex electric field at the aperture	[V/m]
$\mathbf{k}_n$	Fourier mode direction, see equation (2.11)	[–]
ϕ_{ap}	Phase at the aperture	[rad]
ϕ_{target}	Phase model, see equation (2.21)	[rad]
$\psi(t)$	Eikonal, see equation (2.5)	[m]
σ_ϕ	Term in the optimization representing the phase error	[–]
σ_{dir}	Term in the optimization representing the ray direction error	[–]
$\tilde{n}$	Distribution of the refractive index, see equation (2.11)	[–]
ε_i	Permittivity of spherical inclusions, see equation (2.2)	[F/m]
ε_m	Permittivity of matrix, see equation (2.2)	[F/m]
ε_r	Relative permittivity	[–]
ε_{eff}	Effective permittivity	[F/m]
$\vec{r}_{ap}$	Reference position on the aperture	[m]
c	Gyroid Half-thickness , see equation (3.2)	[–]
c_n	Complex Fourier coefficient, see equation (2.11)	[–]
I	Identity matrix	[–]
k_0	Free space wavenumber	[rad/m]
l	Side length of the flat lens	[m]

n	Refractive index	[−]
n_λ	Number of wavelengths, see equation (2.3)	[−]
$N_{rays,ap}$	Number of rays which reach the aperture, see equation (2.16)	[−]
N_{rays}	Total number of rays fired from the source, see equation (2.16)	[−]
$r(t)$	Current position of the ray, see equation (2.5)	[m]
t	Optical length	[m]
t	Thickness of the flat lens, see equation (3.5)	[m]
V_{lens}	Volume of the lens	[m^3]
$y(t)$	State of a given ray, parametrized by the optical length t, see equation (2.5)	[−]
u_{target}	Target direction of the outgoing ray, see equation (2.17)	[−]

Contents

Preface i

Summary ii

Acronyms iii

Nomenclature iv

1 Introduction 1
- 1.1 Motivation . . . 1
- 1.2 Literature Review . . . 2
  - 1.2.1 Microwave Lenses - Historical Perspective and State of the Art . . . 3
  - 1.2.2 Additive Manufacturing of Gradient Index Lenses . . . 4
  - 1.2.3 Lenses for Phased Array Antennas . . . 6
  - 1.2.4 Overview . . . 7
- 1.3 Research Framework . . . 9
  - 1.3.1 Scope . . . 9
  - 1.3.2 Research Questions . . . 10
  - 1.3.3 Novelty of this Work . . . 11
- 1.4 Outline of the Thesis . . . 11

2 Modelling & Simulation 12
- 2.1 Additive Manufacturing of GRIN Media . . . 12
  - 2.1.1 Effective Medium Theory . . . 12
  - 2.1.2 Synthesizing GRIN Media . . . 13
  - 2.1.3 Material and Technology . . . 14
- 2.2 GRIN Lens Antenna Analysis - 'The Forward Problem' . . . 15
  - 2.2.1 Lens Antenna Analysis . . . 16
  - 2.2.2 Ray Optics in GRIN media . . . 17
- 2.3 Optimization of GRIN Lenses - 'The Inverse Problem' . . . 19
  - 2.3.1 Parametrization of GRIN Lenses . . . 19
  - 2.3.2 Optimization . . . 21

3 Results & Measurements 25
- 3.1 3D printing . . . 25
- 3.2 Permittivity Measurements of PLA . . . 26
- 3.3 Validation Case: Optimization of a Luneburg Lens . . . 28
- 3.4 Optimization of a Scan-Enhancing Flat GRIN Lens . . . 30

4 Conclusions 35
- 4.1 Conclusions . . . 35
- 4.2 Recommendations for Future Work . . . 37

References **39**

A Mathematical Conventions **43**

B Derivation of Ray Optics **44**

C On the Phase Model ϕ_{target} **49**

1

Introduction

1.1. Motivation

Over the last 50 years, phased array antennas have become a key element of our wireless telecommunications infrastructure. Some examples include Starlink satellite internet receivers, Viasat in-flight WiFi systems, and Galileo navigation antennas, all shown in Figure 1.1; it is no understatement to say that hundreds of millions of people rely on phased array antennas in their daily lives.

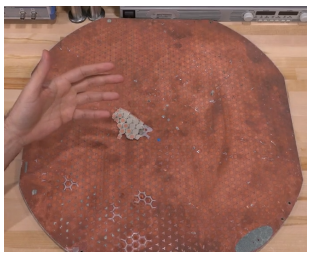

(a) Starlink receiver antenna PCB (courtesy of TheSignalPath).

(b) Viasat in-flight connectivity antenna (courtesy of ESA).

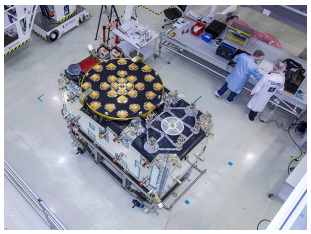

(c) Galileo FOC satellite at ESTEC (courtesy of OHB, ESA).

Figure 1.1: Examples of aerospace applications of phased array antennas

Phased array antennas consist of an array of individual antenna elements. When radiating together, these allow for the synthesis of a highly directive beam, which can be steered by introducing a progressive phase shift along the elements. Phased array antennas (also referred to as phased arrays or electronically steered antennas) offer significant advantages over traditional mechanically-steered antennas. Aside from the obvious benefit of reducing the number of moving parts, phased array antennas can rapidly steer between multiple targets, enabling multiple input/multiple output (MIMO) communication and sensing [1].

However, there are inherent challenges and limitations associated with phased arrays. Notably, a drop in the antenna gain is typically observed when scanning the beam away from broadside, a phenomenon known as 'scan loss'. It is also possible for unintended lobes to form away from the scan direction (known as grating lobes) [2], as shown for example in Figure 1.2. In practice, these effects impose a limit on the scan coverage of the antenna.

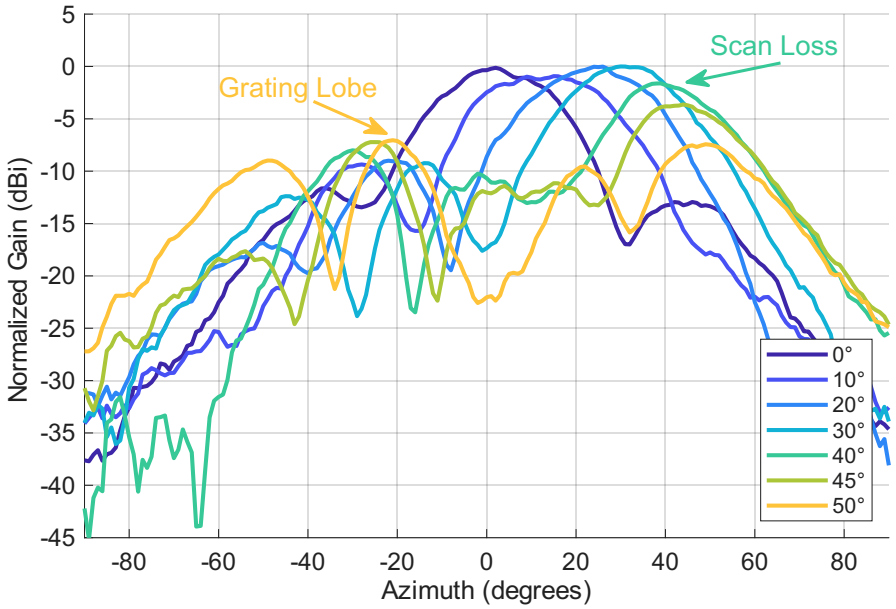

Figure 1.2: Antenna patterns of the TMYTEK BBox 5G phased array antenna at 28GHz. As the steering angle increases, the peak gain decreases, and a grating lobe begins to appear at $-25°$.

There are several approaches to mitigate scan losses of phased array antennas. One approach is to design phased array using broad-beam antenna elements, reducing the scan loss due to the element pattern [3]. Another approach is via the use of conformal (or non-planar) arrays [4], reducing scan losses in large arrays due to the more constant projected area of the array.

However, these approaches are centered on the design of the antenna array itself. An attractive options to enhance the scan coverage of phased arrays is therefore via the use of dielectric lenses, as it would allow for drop-in improvements to existing antennas. It has been shown that dielectric domes have the potential to enhance the scan range of phased array antennas [5]. With recent advances in additive manufacturing, it is possible to realize lenses with a spatially varying refractive index, allowing more freedom in the form factor of such lenses [6].

Lenses with a spatially varying refractive index, also known as Gradient Index (GRIN) lenses, are not a new idea; in fact, GRIN media has been the subject of extensive research in optics [7]. The application of GRIN lenses to antennas is a relatively recent development, enabled by progress in additive manufacturing and a shift towards shorter wavelengths in microwave engineering. However, the design and realization of such lenses remains challenging, and few methods have been presented to optimize arbitrarily varying GRIN profiles. In this thesis, we investigate the design and optimization of GRIN lenses to enhance the usable scan range of phased array antennas.

1.2. Literature Review

To begin, we present a review of scientific literature on microwave lenses, GRIN lenses, and their applications to phased array antennas.

We first present a brief history of lens antennas, followed by a short overview of state of the

art and current trends. We then focus on GRIN lenses, followed by the application of lenses to antenna arrays.

1.2.1. Microwave Lenses - Historical Perspective and State of the Art

The earliest microwave lenses were constructed by physicists in the late 19th century; Jagadish Chandra Bose published results on a sulfur lens designed to collimate millimeter waves in 1896 [8], only 9 years after electromagnetic waves had been experimentally observed by Heinrich Hertz. Several other physicists developed microwave lenses during this time, aiming to better understand the newly discovered electromagnetic waves.

Interest in lens antennas then declined during the development and commercialization of the radio. Lenses must be physically larger than the wavelength of light to be effective, making them impractical for low-frequency radio applications. There was some renewed interest during the second world war with the development of radar, where frequencies up to $10\,\mathrm{GHz}$ became commonplace.

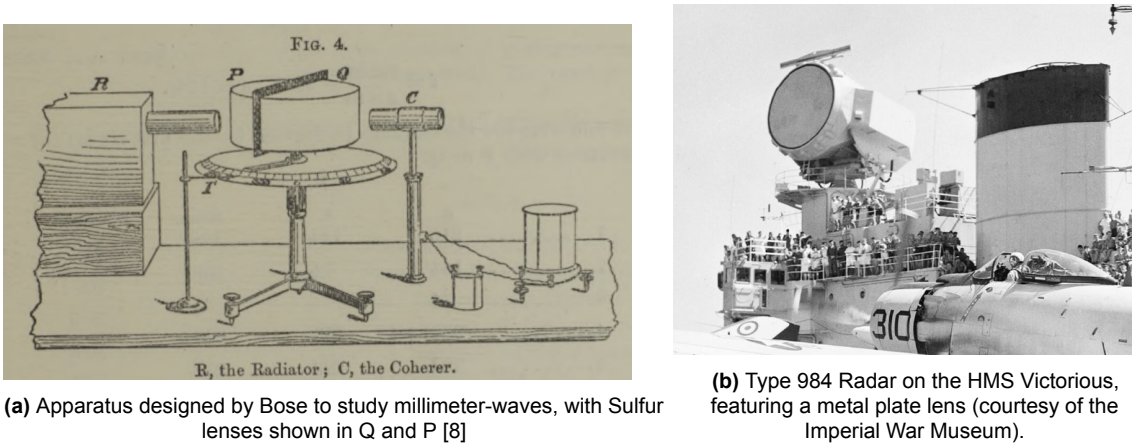

(a) Apparatus designed by Bose to study millimeter-waves, with Sulfur lenses shown in Q and P [8]

(b) Type 984 Radar on the HMS Victorious, featuring a metal plate lens (courtesy of the Imperial War Museum).

Figure 1.3: Notable early microwave lenses

To obtain higher bandwidths and allow for miniaturization, communications standards have been gradually shifting towards higher frequencies (i.e. shorter wavelengths), resulting in significant renewed interest in lens antennas in the past decade, as evidenced by the volume of publications shown in Figure 1.4.

Lens antennas are typically electrically large (i.e. much larger than the wavelength). Thus, full-wave simulations of lens antennas are often highly computationally expensive. There is therefore significant interest in developing more efficient methods to analyze the radiation of lens antennas, including methods based on physical optics [9] and method of moments solvers [10].

Another topic of interest is that of switched-beam antennas. Since the beam of a lens antenna can be steered by only displacing the feed, it is possible to build a high gain beamforming antenna without the use of phase shifters, significantly reducing the cost and complexity over phased arrays. These improvements are at the expense of limited control over the radiation pattern, and are especially interesting for cost-driven applications, such as automotive radar [11] [12].

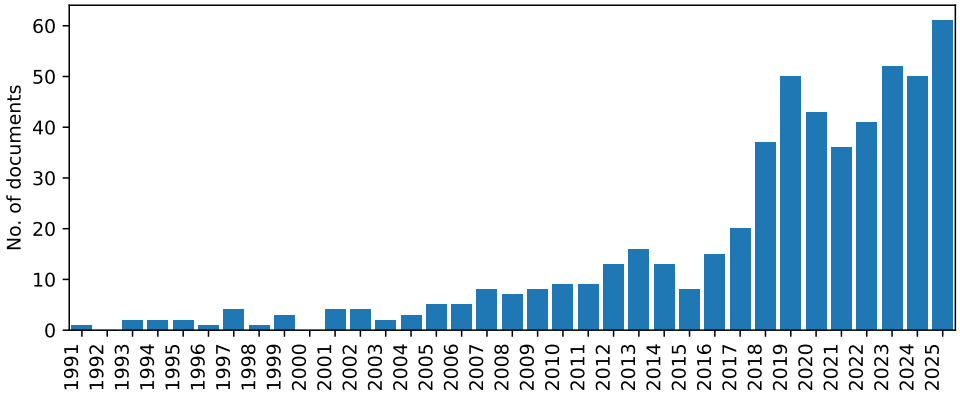

Figure 1.4: Journal publications by year on IEEE Xplore between 1990-2025 with both the terms 'lens' and 'antenna' in the publication title.

For an example of the current state of the art of the design, modeling and applications of dielectric lens antennas in millimeter wave to terahertz frequencies, readers are encouraged to consult the PhD dissertation of Huasheng Zhang [13]. One example of a lens antenna array developed within this dissertation is shown for reference in Figure 1.5; operating at $24\,\mathrm{GHz}$ to $30\,\mathrm{GHz}$, the lenses enable grating lobe suppression with an array spacing of $2\lambda_0$.

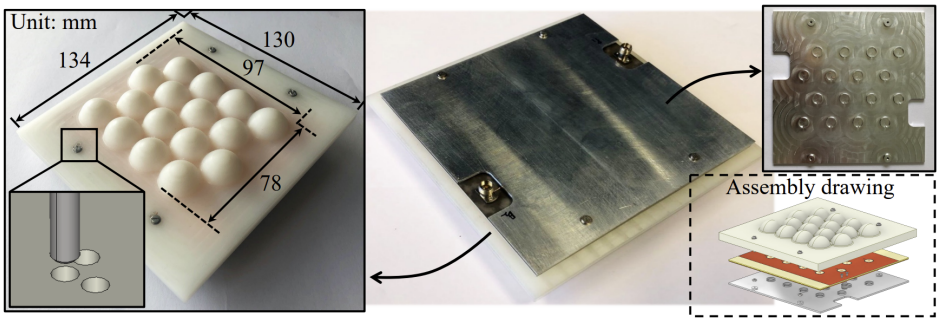

Figure 1.5: Lens Phased Array antenna, from Zhang's 2024 dissertation [13].

1.2.2. Additive Manufacturing of Gradient Index Lenses

Media with a spatially varying refractive index, often refered to as Gradient Index (GRIN), have been studied since the 19$^{\text{th}}$ century by physicists and mathematicians, though their application in microwave engineering is a more recent development.

One early example of a gradient index lens which is worth mentioning here is the Luneburg lens. Discovered by mathematician Rudolf Luneburg in 1944, this spherically symmetric lens collimates light to a point on the surface [7]. This lens has a number of interesting mathematical properties, including a remarkably simple distribution of the refractive index, as shown in Equation 1.1.

$$n(r) = \sqrt{2 - \left(\frac{r}{R}\right)^2} \tag{1.1}$$

In Equation 1.1, R is the radius of the lens, and r is the partial radius at a point inside the lens. The Luneburg lens is particularly useful as a validation case, as will discussed in the following chapters.

The design of GRIN lenses remains challenging. Simple lenses may be designed directly using Fermat's principle, as was done by Luneburg for his eponymous lens. Another common technique is the use of Transformation Optics (TO), where a coordinate transform is defined describing the desired path of light rays. This coordinate transform is then absorbed into the material properties, allowing for the design of metamaterial-based optical devices [14].

Though powerful, TO can result in GRIN profiles which are difficult to realize, including anisotropic media, and media with negative refractive index. While this is obviously not feasible with simple dielectrics, it can be achieved using periodic metal structures, typically referred to as metasurfaces and meta-atoms [15]. Quasi-Conformal Transformation Optics (QCTO) methods have also been proposed to design lenses with isotropic refractive index using TO [16].

There have been relatively few attempts to optimize lenses with an arbitrarily varying GRIN profile. One notable example is presented by Budhu et al. in [17], where the authors defined the GRIN profile using a 2D cubic spline surface, shown in Figure 1.6. The GRIN profile was optimized using particle swarm optimization, a popular technique for electromagnetics problems [18]. A similar approach was used by Xu et al. [19], where the GRIN profile was defined with a 2D Bezier surface. While these techniques to parametrize the GRIN profiles are effective, they have a few drawbacks. Namely, they do not directly account for the maximum/minimum permittivity set by the manufacturing constraints, and are more difficult to extend to a 3D varying GRIN profile, requiring significantly more optimization parameters.

Other attempts to optimize GRIN profiles have limitations; namely, [20] featured a very limited search space, with only one parameter included in the optimization, and other attempts use multiple discrete sections, optimizing the shape of each section instead of a continuously varying GRIN profile, for example in in [21] and [22].

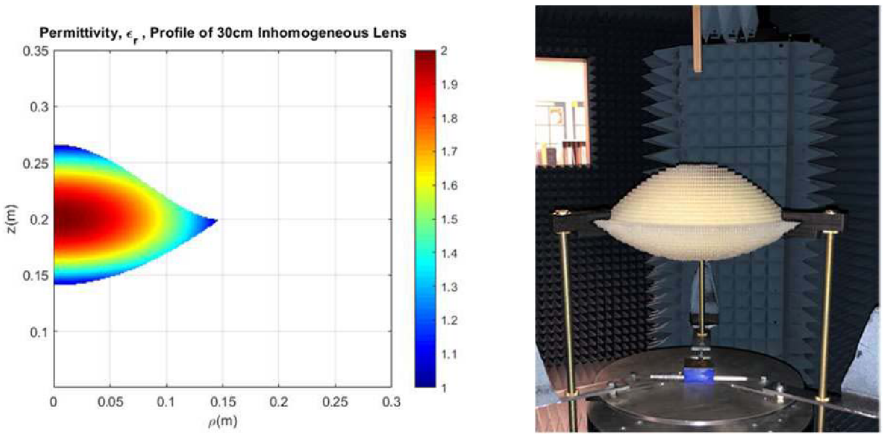

Figure 1.6: Optimized of a GRIN lens with an arbitrarily varying GRIN profile, from [17]. The GRIN profile is defined by a 2D cubic spline, which is then revolved about the x axis.

Until the commercialization of additive manufacturing, realizing GRIN media was challeng-

ing, often requiring the use of multiple materials with different permittivities. Advances in additive manufacturing allow for the synthesis (i.e. generating the geometry) and fabrication of materials with continuously graded density [23], as further discussed in section 2.1.

A wide range of additive manufacturing technologies have been proposed to fabricate GRIN structures, including exotic techniques such as jet binding in [17], direct ink writing loaded with dielectric powders [24] and sintered ceramics [25] [26]. One technology which is notably sparse in literature is resin printing, as most photopolymer resins have unacceptably high losses for use in microwave engineering. At the time of writing, only one low-loss resin is commercially available, designed by Fortify3D and Rogers corporation for use with proprietary printers.

One particularly helpful reference on 3D printed GRIN lenses is the comprehensive 2023 review by Munina et al. [6]. Another useful reference is the PhD dissertation of Hehenberger [27], focusing on the synthesis, homogenization and modeling of GRIN media based on dielectric crystals.

1.2.3. Lenses for Phased Array Antennas

As discussed above, microwave lenses may be used to create switched-beam antennas, allowing for beam steering without the use of phase shifters. There has been comparatively little attention on the design of lenses for use in combination with phased array antennas.

Several works have proposed the use of a dielectric dome to enhance the scan range of a phased array. For example, the dielectric dome shown in Figure 1.7 offers an angular scan enhancement of $10°$ to a circularly polarized phased array at $29\,\mathrm{GHz}$. Similarly, a dome lens with quarter-wave matching layers was presented in [28]; in this case, the lens was analyzed using full wave simulations, limiting the optimization to a single parameter (in this case, the height of the dome lens). This dome was also experimentally validated, increasing the gain of a $28\,\mathrm{GHz}$ phased array by $0.4\,\mathrm{dBi}$ at a steering angle of $60°$.

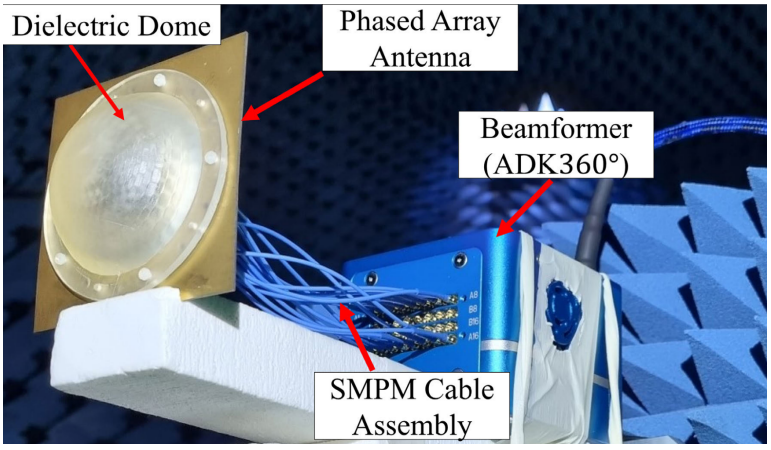

Figure 1.7: Example of a phased array-fed dielectric dome antenna, reprinted from [29]. This solid dielectric dome offers $10°$ of angular scan enhancement to the phased array antenna.

Although full-wave methods are highly accurate, their computational cost restricts the search space of the optimization. A larger search space would be beneficial for more complex, multi-objective optimizations; in this case, it is attractive to make use of more computation-

ally efficient methods, such as ray-tracing and Physical Optics (PO). In [21], the authors implemented a 2D PO algorithm to optimize a multi-layered dielectric dome, where the surface of each layer was defined by a spline. Although these results are not experimentally validated, the multi-layer dome offers a gain enhancement of $1.5\,\mathrm{dBi}$ at $60°$.

The term Phased Array-Fed Lens (PAFL) has recently been coined by Wang [30], adapted from Phased Array-Fed Reflector (PAFR) antennas [31]. In [30], Wang proposed the use of a PAFL to improve the pattern control compared to a switched-beam array lens antenna. However, Wang did not explicitly design the lens for use in with a phased array; rather, the authors showed that a lens designed for switched-beam arrays could be fed by a phased array to achieve finer angular resolution.

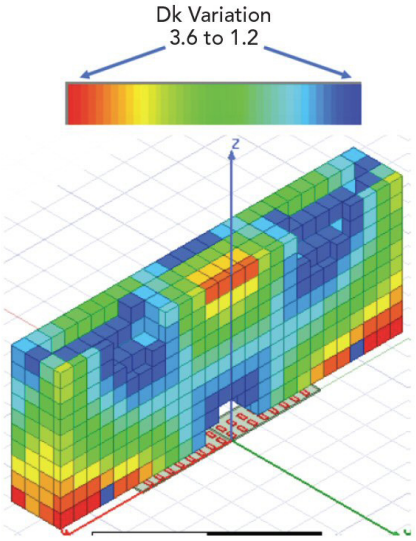

(a) Flat GRIN lens optimized to enhance the scan range of a phased array, from Microwave Journal magazine [32].

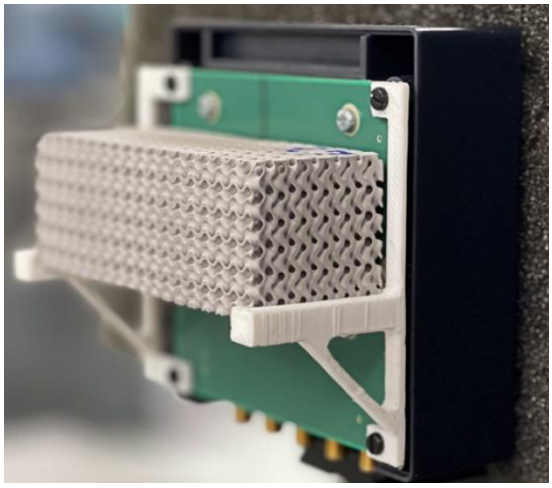

(b) Printed flat GRIN lens, from the corresponding conference paper [33].

Figure 1.8: Flat GRIN lens optimized to enhance the scan coverage of a phased array, designed by Fortify3D and Rogers corporation.

One particularly interesting example of GRIN lenses designed for phased arrays comes from a 2022 article in the Microwave Journal magazine, shown in Figure 1.8. There, the authors presented a flat GRIN lens to enhance the scan coverage of a phased array antenna [32], claiming to increase the field of view up to $90°$. A conference paper was later published on this same lens in [33]. Unfortunately, the authors did not discuss the analysis and optimization procedure, and it is unclear whether the measured performance of the lens (shown in the black dashed line in Figure 3 of [33]) supports the claim of $90°$ scan coverage.

1.2.4. Overview

Although there is an extensive body of research on dielectric lenses and phased array antennas individually, there has been comparatively little research on the application of lenses specifically to phased array systems (and even fewer on GRIN lenses for phased arrays). Most existing studies of phased array-fed lenses focus on homogeneous dielectric domes, while GRIN lenses are more commonly investigated in the context of switched-beam antennas or standalone antenna feeds.

To date, there have been few attempts to optimize lenses with arbitrarily varying GRIN profiles. This can be attributed to practical limitations which have only recently been overcome; Additive manufacturing technology capable of fabricating spatially varying dielectric media at microwave frequencies has only become affordable and accessible in the last two decades [6]. Furthermore, the tools to synthesize 3D printed structures with continuous grading have only recently become available.

As discussed above, there have been relatively few attempts to design GRIN lenses to enhance the scan coverage of phased array antennas. The closest example is likely from the multi-layer dielectric dome presented [21], offering a gain enhancement of $1.5\,\mathrm{dBi}$ at $60°$. However, the multi-layered dome approach offers little freedom on the form factor of the antenna, and the layered structure results in multiple reflections; both of these challenges could be addressed by making use of continuously varying GRIN lenses. Furthermore, the multi-layered dome presented in [21] is not experimentally validated.

As discussed in subsection 1.2.2, there have been a few attempts to optimize continuously varying GRIN profiles. One notable examples was presented by Budhu et al. in [17]. Here, the authors parametrized the GRIN profiles using on 2D spline surface. Although this is a straightforward approach, offers a limited search space, and does not directly account for limits imposed by the manufacturing process.

Relevant papers were collected using the Zotero citation management tool. A total of 108 records were categorized as relevant to this thesis. Of these, 89 are journal articles and conference papers; the source of these publications is shown in Figure 1.9. We see that GRIN lenses at microwave frequencies are most frequently published in IEEE Transactions on Antennas and Propagation (IEEE TAP); It should be noted that there is also a significant volume of literature on lens antennas in IEEE Transactions on Terahertz and Technology, although GRIN lenses are rarely treated there, as it is significantly more difficult to fabricate GRIN media at terahertz frequencies.

Although the Microwave Journal online article mentioned in subsection 1.2.3 was one of the inspirations behind this thesis topic, this source was not used extensively, as the authors provide very few details on the optimization and modeling. Instead, the papers listed below were used extensively throughout this thesis, and are worth specifically highlighting:

- Budhu et al.'s 2019 paper on GRIN lens design and optimization [17]. The authors present a Particle Swarm Optimization (PSO) algorithm to optimize a switched-beam GRIN lens antenna. We employ a similar optimization procedure here, with a different optimization goal and a novel parametrization for the GRIN profile.
- Gashi et al.'s 2022 paper on propagation in GRIN media [9]. Here, the authors present a method to compute the electric field propagation in GRIN media using a single vectorial ODE, which we replicated and used in our optimization.
- Hehenberger's 2025 PhD dissertation on dielectric crystal-based GRIN media [27], as a general reference for modeling, synthesizing and fabricating GRIN media based on dielectric crystals for use at microwave frequencies.

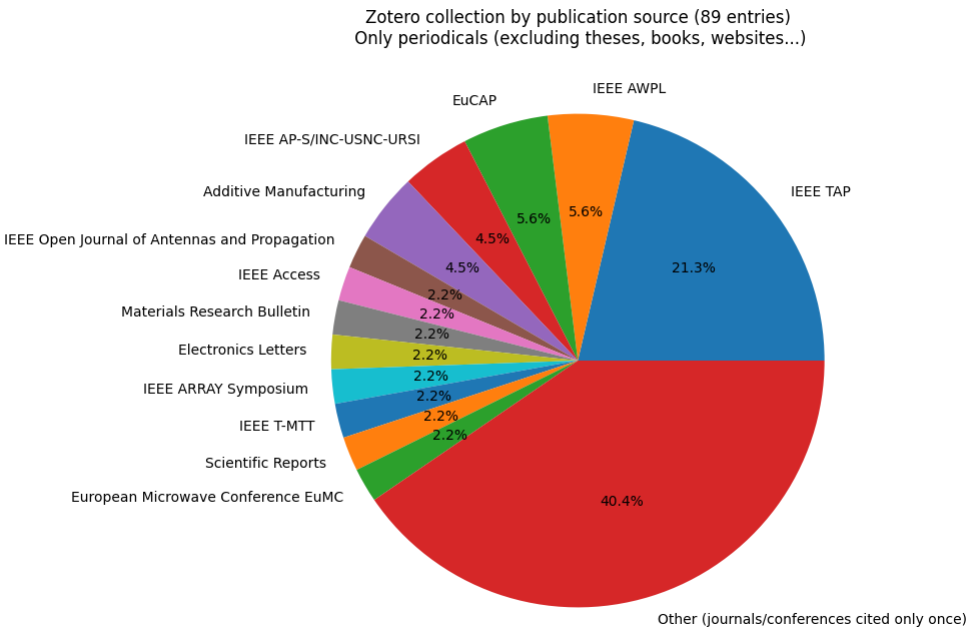

Figure 1.9: Pie chart of publication source for papers included in this literature study.

1.3. Research Framework

Here, we present the goals of this research, as well as the assumptions and limitations. We then outline the research questions, and highlight the novel elements of this research.

1.3.1. Scope

The goal of the project is to design a flat GRIN lens to enhance the scan coverage of a phased array antenna. This includes modeling, optimization and fabrication of the lens. It is planned to perform experimental validation using a TMYTEK BBox 5G phased array antenna operating at $28\,\mathrm{GHz}$ in the Delft University Chamber for Antenna Tests (DUCAT) facility. As this antenna is relatively narrow-band, we neglect the frequency dependence of the permittivity of the material.

The DUCAT facility features two motorized turntables for antenna pattern measurements. Although the full 2D radiation pattern could be measured by tilting the antenna under test, doing so takes considerably more time. To simplify the optimization and reduce the measurement time, we limit the optimization to the scan coverage in one cut plane.

As will be discussed in subsection 2.1.3, FFF offers a convenient and low-cost method to realize GRIN media. Other additive manufacturing techniques are either too complex, or produce media with high dielectric losses. Thus, we choose to only consider GRIN media using dielectric crystals, printed using FFF (although we acknowledge that there are many more ways to realize GRIN media).

Since the BBox features a relatively small array (4x4 elements), it is convenient to place the lens in the far-field of the array. This allows us to model the array as a point source, as well as minimizing the effect of reflections reflections from the lens. There are other challenges associated with placing the lens in the near-field of the array elements; namely, this would disturb the effective spacing between the elements, which would be significantly

more challenging to model.

Taking the Fraunhofer distance as the beginning of the far field, we find that the lens should be placed a distance of at least $4.5\,\mathrm{cm}$ from the array. This poses a challenge; to capture a large portion of the radiated power, the flat lens should be very wide, as shown in the scale drawing in Figure 1.10. Taking the maximum print size of $20\,\mathrm{cm}$ for an Original Prusa Mk4 printer, we see that the lens entry captures a maximum of $66°$ of the radiation, modeling the array as a point source. This should still produce acceptable results, considering that the TMYTEK BBox array advertises a maximum steering angle of $45°$.

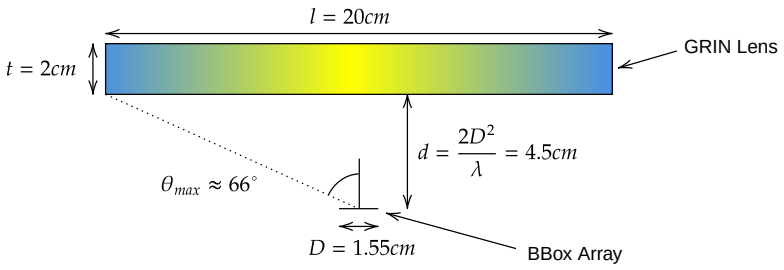

Figure 1.10: Diagram of a $20\,\mathrm{cm}$ wide flat lens in the far-field of the array, drawn to scale.

1.3.2. Research Questions

This project is divided into two research questions. The first research question pertains to the 3D printing of GRIN media:

> **RQ1: How can GRIN media for use at microwave frequencies be realized using single-material Fused Filament Fabrication (FFF) 3D printing?**

This question is divided into the following sub-questions:

RQ1.1: Which computational tools are best suited to synthesize air-dielectric GRIN media for use at microwave frequencies?

RQ1.2: How can FFF filaments be selected and characterized for use in GRIN lenses at microwave frequencies?

RQ1.3: How do manufacturing constraints arising from the FFF process impact the design of gradient index lenses?

The second research question is focused on the electromagnetic analysis, design and optimization of GRIN lenses:

> **RQ2: How can GRIN lenses be designed and optimized to increase the scan coverage of a practical planar phased array antenna?**

This is again divided into two sub-questions:

RQ2.1: Which computational electromagnetics methods are suited to the analysis of GRIN lenses in optimization workflows?

RQ2.2: Which simplifying assumptions can be made without significantly degrading accuracy when analyzing the effect of GRIN lenses on phased array antennas?

1.3.3. Novelty of this Work

The following novel developments are presented in this work:

- A new parametrization of GRIN media is developed, based on a Fourier series distribution of the refractive index scaled to the achievable limits set by the manufacturing process.
- Using this parametrization, we show that lenses can be designed & optimized GRIN lenses using a small number of GO rays, greatly reducing the computational effort and allowing for a larger solution space over PO/full wave methods.
- A flat GRIN lens to enhance the usable scan range of a practical phased array antenna is fabricated and experimentally validated, increasing the scan envelope by $\pm 10^{\circ}$ and demonstrating the drop-in improvement capability of such dielectric lenses.

One development also worth highlighting here is the use of continuously varying TPMS structures to realize GRIN media. Although graded TPMS structures have been applied to GRIN lenses in industry (most notably by Fortify3D), the tools to synthesize such structures had not been previously reported in the microwave lens literature.

1.4. Outline of the Thesis

The remainder of this thesis is structured as follows.

First, the realization of 3D printed media with spatially varying refractive index is discussed in section 2.1. Next, the analysis and optimization of GRIN lenses are presented in section 2.2 and section 2.3 respectively.

Measurements of the volume fraction and permittivity of 3D printed GRIN media are reported in section 3.1 and section 3.2 respectively. The results of the optimization of the flat GRIN lens are presented in section 3.4, together with antenna pattern measurements. This optimization method was also validated by optimizing and testing a Luneburg lens, as outlined in section 3.3.

The conclusions of this thesis are presented in section 4.1, followed by recommendations for further research in section 4.2.

2

Modelling & Simulation

2.1. Additive Manufacturing of GRIN Media

It is not obvious at a glance how media with a varying refractive index can be realized with 3D printing. Here, we discuss the theory and implementation of gradient index media using dielectric crystals with a sub-wavelength unit cell.

Readers may note that the terms 'permittivity' and 'refractive index' are used in the same context in this section. These quantities are distinct but related; the relative permittivity ε_r is a measure of how much a medium is polarized by an electric field. The refractive index n is a measure of how much an electromagnetic wave slows down in a medium. In a non-magnetic medium, these quantities are related by Equation 2.1.

$$n = \sqrt{\varepsilon_r} \tag{2.1}$$

There is good reason why both of these quantities are used; the use of ε_r is more convenient in effective medium theory, whereas n is more convenient in optics. In any case, since optical components are almost never magnetic, Equation 2.1 can generally be used.

2.1.1. Effective Medium Theory

For illustration, let us consider a polystyrene foam. Polystyrene has a permittivity of ~ 2.6, and air has a permittivity of ~ 1. If the foam is composed of $5\,\%$ polystyrene by volume, we can logically expect the foam to have a permittivity close to 1.08, applying a linear rule of mixtures.

Several models have been developed to compute the permittivity of such mixtures, grouped under the umbrella term 'Effective medium theory'. A well-known example is as the Maxwell Garnett approximation[34], shown in Equation 2.2. Here, the mixture is modeled as small spherical inclusions with permittivity ε_i and volume fraction δ_i, suspended in a host matrix ε_m. For low permittivity contrasts, the Maxwell Garnett approximation is fairly close to a linear rule of mixtures, as shown in Figure 2.1.

$$\varepsilon_{eff} = \varepsilon_m \frac{2\delta_i(\varepsilon_i - \varepsilon_m) + \varepsilon_i + 2\varepsilon_m}{2\varepsilon_m + \varepsilon_i - \delta_i(\varepsilon_i - \varepsilon_m)} \tag{2.2}$$

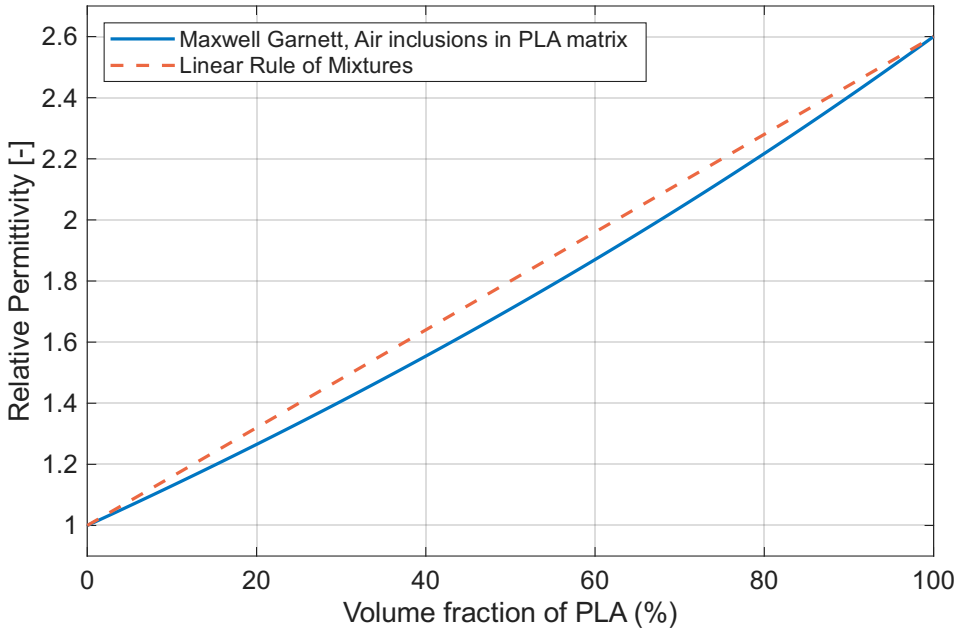

Figure 2.1: Comparison of a linear rule of mixtures and the Maxwell Garnett approximation, using Equation 2.2 with $\varepsilon_m = 2.6$, $\varepsilon_i = 1$.

Importantly, effective medium theory is only valid if the features of the mixture are small. Continuing with the example of polystyrene foam, the cells of the foam should be much smaller than the wavelength for the medium to behave as though it was homogeneous with permittivity ε_{eff}.

The Maxwell Garnett approximation is a relatively simple model, and is known to be inaccurate for mixtures with both high permittivity contrast and high volume fractions. Furthermore, it cannot be used to predict frequency-dependent effects. More advanced techniques, such as plane wave expansion methods and Floquet port simulations, have been proposed to model these effects [35]. The proposed use case in this thesis permits the use of the Maxwell Garnett relation, as the selected material has a reasonably low permittivity contrast with air (see subsection 2.1.3).

One aspect to consider is anisotropy; Hehenberger showed that the layers from the FFF process result in an anisotropic medium, with slightly lower permittivity in the direction normal to the layers [36]. Looking closely at the results, we see that the anisotropy is minimal for materials with low bulk permittivity. To simplify the subsequent modeling and analysis, we assume that the material is isotropic. If this work was to be repeated with high-permittivity materials, it may be possible to synthesize isotropic media by scaling the dielectric crystal in the directions of the layers (i.e. 'flattening' the crystal), as was also investigated in [36].

2.1.2. Synthesizing GRIN Media

In essence, GRIN media can be realized by 3D printing structures with spatially varying density. The most common approach employed within microwave GRIN lens literature is

via unit cell with parametrized thickness, of which some examples are shown in Figure 2.2. So long as the unit cell size is much smaller than the wavelength, the resulting medium behaves as though it was a homogeneous medium with permittivity ε_{eff}.

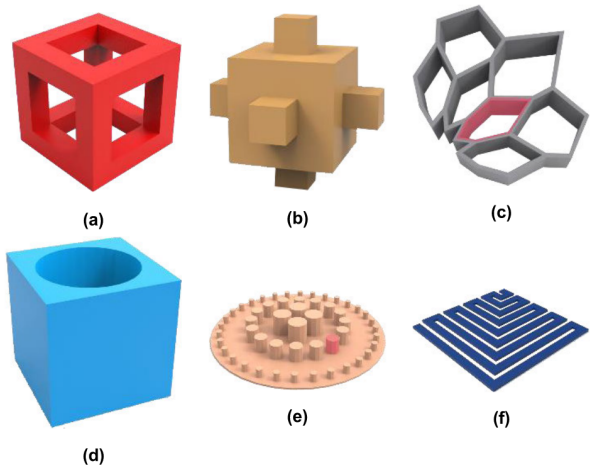

Figure 2.2: Example of parametric unit cells typically used to realize all-dielectric GRIN lenses, from [6].

This parametric unit cell approach has a few downsides; most notably, the density grading is not truly continuous, but discretized to the unit cell dimensions. Several methods have been proposed to realize continuously varying materials; for example, Hehenberger made use of the Spatially Variant Lattice (SVL) Algorithm [37], which allows for the synthesis of structures with spatially controlled density, unit cell size and orientation. While extremely powerful, this algorithm is very computationally expensive, and is thus limited to relatively small and simple structures.

A promising approach to realize continuously graded structures is via the use of Triply Periodic Minimal Surface (TPMS) structures. These are commonplace in the additive manufacturing community, and several tools to synthesize spatially varying TPMS lattices have recently become available, including LisbonTPMS [38], LatticeWorks [39] and nTopology [1]. In our use case, the LisbonTPMS library is convenient, as it is both lightweight and powerful, allowing for the synthesis of graded TPMS structures directly using a python function.

Gyroids are a particularly interesting class of TPMS structures, as they are mechanically strong, isotropic and easy to print. Furthermore, gyroid surfaces can be efficiently synthesized, as they can approximated by a simple trigonometric equation. An example of a graded gyroid structure generated using LisbonTPMS is shown in Figure 2.3. Further details on the 3D printing of such structures are discussed in section 3.1.

2.1.3. Material and Technology

As discussed in subsection 1.3.1, we choose to limit the scope of this research to single-material FFF. Even so, not all thermoplastic filaments are born equal; we will here motivate this decision, and compare some common 3D printing materials.

Looking at Figure 2.4, we see that Polypropylene (PP) and silica ceramics are promising materials for microwave applications, due to the exceptionally low loss tangent. The permit-

[1] see `https://www.ntop.com/`, accessed 9 December 2025

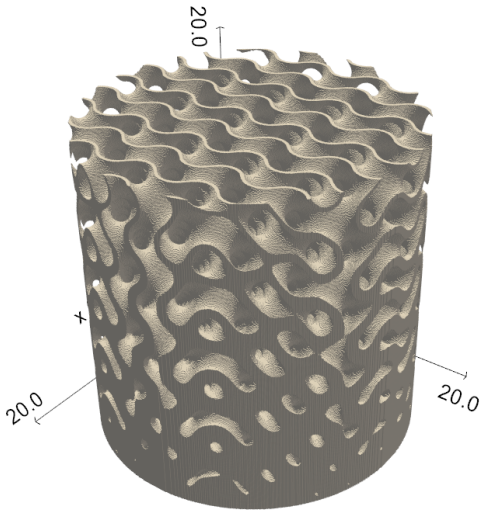

Figure 2.3: Graded Gyroid structure generated using LisbonTPMS; Note the smoothly varying wall thickness.

tivity can be increased by doping PP with high permittivity ceramic powders; Such filament seems to be available commercially under the brand name Zetamix epsilon, though the datasheet only describes the polymer as a polyolefin [40]. Unfortunately, Polypropylene is notoriously difficult to print, especially for large structures.

On the other end of the spectrum, Polylactic Acid (PLA) is an attractive option, despite the unimpressive loss tangent. PLA is widely available, significantly cheaper, and easier to print compared to the other materials shown on Figure 2.4. To decide whether PLA is acceptable, and provide some intuition on the impact of the loss tangent, we plot the power loss per wavelengths for different materials in Figure 2.5. The power loss over n_λ wavelengths is shown in equation Equation 2.3

$$\text{Power dissipated (\%)} = 100 \cdot (e^{-2\pi n_\lambda \tan(\delta)} - 1) \tag{2.3}$$

The wavelength at our design frequency of $28\,\mathrm{GHz}$ is approximately $1.1\,\mathrm{cm}$; Thus, we expect the optical path length within the lens to be no more than 10 to 20 wavelengths. This would result in $1.5\,\mathrm{dB}$ to $3\,\mathrm{dB}$ of dielectric losses; while this would likely be unacceptably high for use a real system, it is sufficient for a demonstration. Figure 2.5 also highlights the need for low-loss dielectrics, especially for high-frequency applications.

2.2. GRIN Lens Antenna Analysis - 'The Forward Problem'

Several methods have been developed to model the radiation of lens antennas at microwave frequencies. We first discuss the accuracy and computational effort of these different methods, after which we describe the curved ray-tracing method outlined by Gashi et al. [9].

David Davidson's book "Computational Electromagnetics for RF and Microwave Engineering" [42] is used throughout the next subsection; The citation is hereafter omitted.

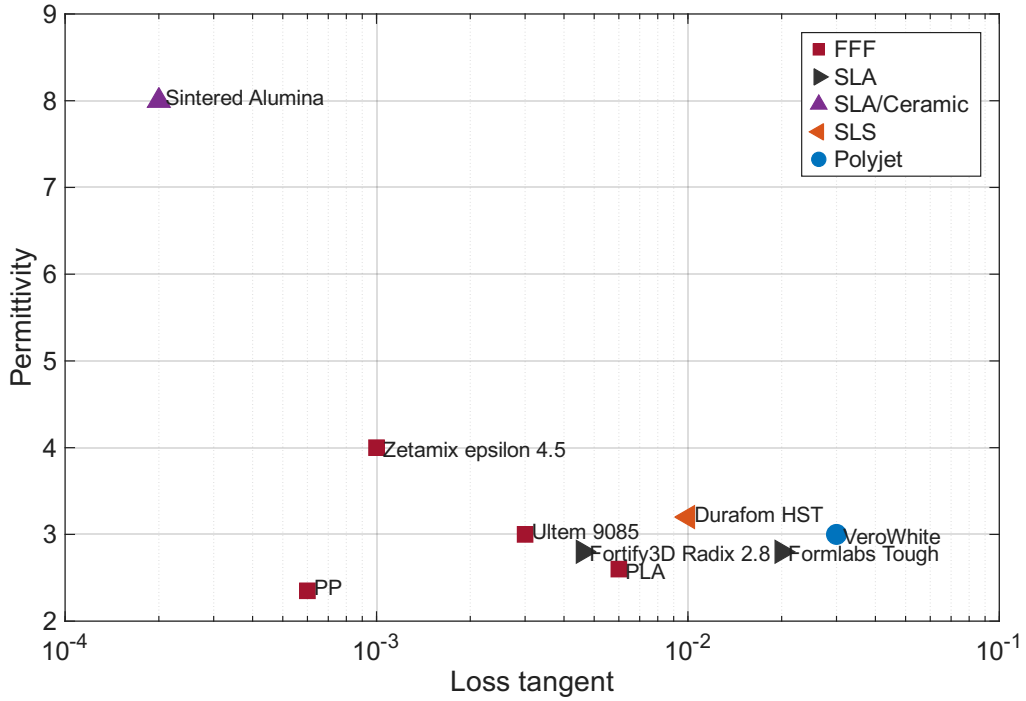

Figure 2.4: Dielectric constant and loss of common 3D printed materials, compiled from [41], Fortify3D promotional material and measurements from IT'IS (see section 3.2).

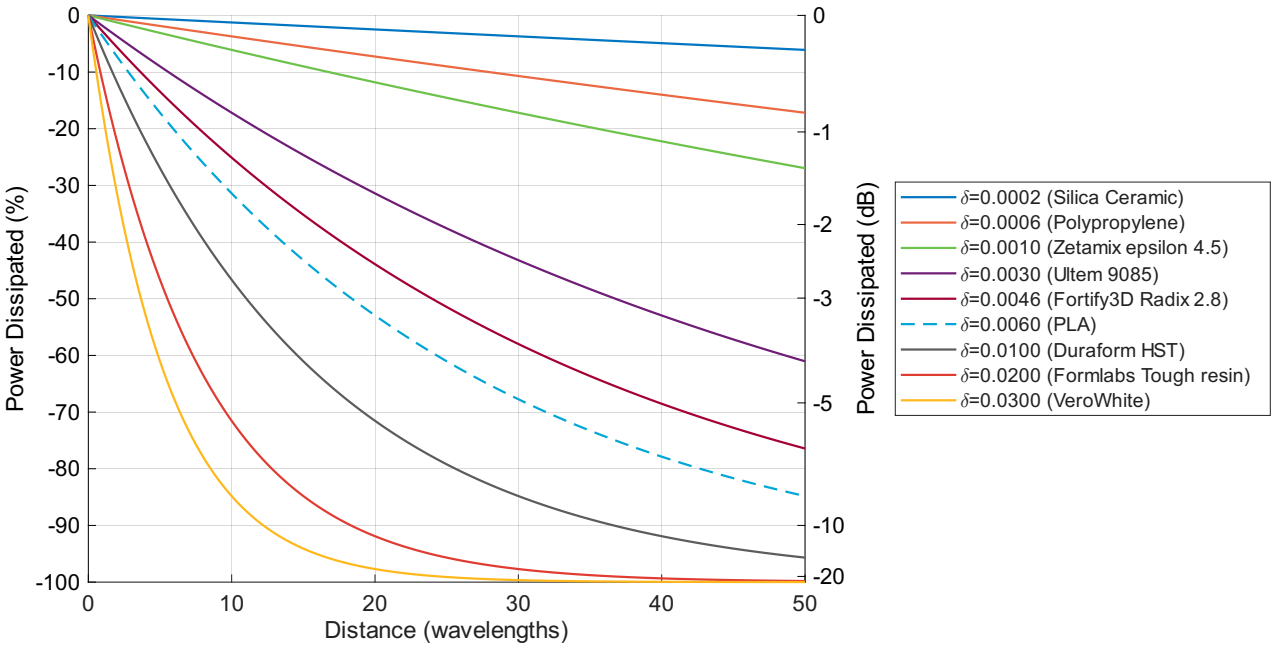

Figure 2.5: Power dissipated by dielectric losses against distance for the materials shown in Figure 2.4. Note that this refers to the number of wavelengths traveled in the material (and not in free space).

2.2.1. Lens Antenna Analysis

Lens antennas are often treated as aperture antennas; Assuming that most of the radiation passes through the aperture, the antenna radiation can be computed from the field at the aperture using the surface equivalence theorem, as illustrated in Figure 2.6.

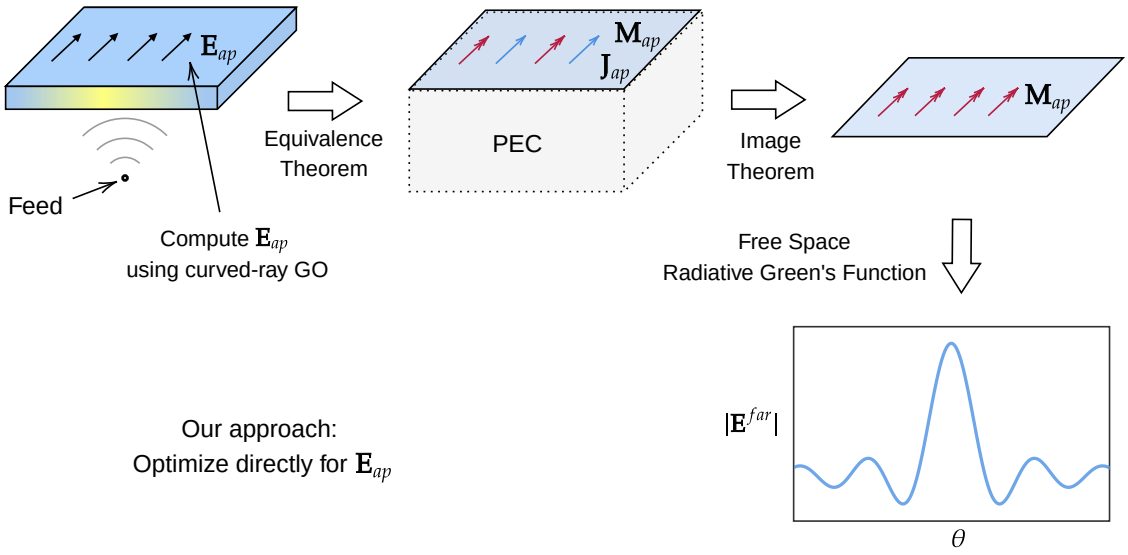

Figure 2.6: Example of physical optics analysis for an inhomogeneous lens. In this work, we optimize directly for the equivalent currents at the aperture, skipping the computation of the radiated field.

This can be divided into two problems; computing the field at the aperture, and computing the resulting radiated far-field. In some idealized cases, this can be done entirely analytically, though this is generally not the case for GRIN lenses.

The most accurate (and most computationally expensive) methods are full-wave simulations, where Maxwell's equations are solved without any simplifying physical assumptions. Full-wave methods include Method of Moments (MoM), Finite Difference Time Domain (FDTD) and Finite Element Modelling (FEM). While accurate, these techniques are often very computationally expensive for electrically large antennas (where the antenna dimensions $d \gg \lambda_0$).

As wavelengths approach optical frequencies, full-wave simulations become impractical. In these cases, Physical Optics (PO) methods may be used. In this case, Geometrical Optics (GO) is used to compute the field at the aperture, after which the radiated far-field is computed with a spatial Fourier transform of the equivalent currents at the aperture. As discussed in subsection 2.2.2, the GO approximation is only valid at high frequencies.

A brief aside on physical optics; the above definition is broadly used in the computational electromagnetics community. Within the optics and physics community, physical optics (also referred to as wave optics) refers more generally to the extension of geometrical optics to account for wave-like properties of light.

For this thesis, we opt for an optimization algorithm similar to [17], using the curved ray optics method outlined in [9], described in the following subsection.

2.2.2. Ray Optics in GRIN media

In Geometrical Optics, the electric field is described by Equation 2.4, where $\psi(\mathbf{r})$ is the eikonal, a scalar function which represents the optical path.

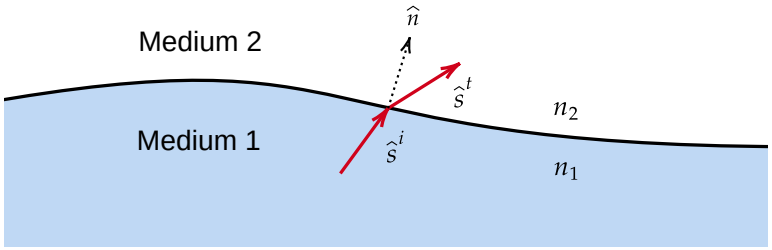

Figure 2.7: Diagram of the lens-air interface, for use with Equation 2.6

$$\mathbf{E}(\mathbf{r}) = \mathbf{E}_0(\mathbf{r})e^{-jk_0\psi(\mathbf{r})} \tag{2.4}$$

From Equation 2.4 and Maxwell's equations, we can derive a system of ODEs for the optical rays. This derivation highlights the assumption that k_0 is large, as discussed in Appendix B.

The propagation of an optical ray is described by Equation 2.5, where $\nabla\psi$ is the gradient of the eikonal, equivalent to a unit vector in the ray direction multiplied by the refractive index $n\hat{s}$. The system of ODEs is parametrized by the optical length along the ray t.

$$y(t) = \begin{bmatrix} r(t) \\ \nabla\psi(t) \end{bmatrix}, \; y'(t) = \begin{bmatrix} \nabla\psi(t)/n^2 \\ \nabla n/n \end{bmatrix}. \tag{2.5}$$

After selecting the initial ray position & direction $r(0)$ and $\nabla\psi(0)$, we can then (for example) use Runge-Kutta methods to numerically solve the equations, provided that the refractive index n and its gradient ∇n are known. In this work, we make use of matlab's ode45 solver to solve this system of ODEs without issue.

We also have to account for the discontinuity in the refractive index at the lens-air interface, described by Snell's law. This can be written in vector form as Equation 2.6, where the unit vector $\hat{s}^i$ is the incident ray, $\hat{s}^t$ is the transmitted ray, and $\hat{n}$ is the normal of the surface pointing into medium two (as illustrated in Figure 2.7). It should be noted that the notation $\hat{n}\hat{n}$ refers to the dyadic product, equivalent to vector multiplication between a column vector and a row vector.

$$\hat{s}^t = \frac{n_1}{n_2}\left(I - \hat{n}\hat{n}\right)\cdot\hat{s}^i + \sqrt{1 - \left|\frac{n_1}{n_2}\left(I - \hat{n}\hat{n}\right)\hat{s}^i\right|^2}\,\hat{n}. \tag{2.6}$$

From Equation 2.5, we can compute the phase of the electric field at the aperture, simply given by the optical path length of a ray at the aperture multiplied by the free space wavenumber k_0, as shown in Equation 2.7.

$$\phi_{ap} = k_0 t_{ap} \tag{2.7}$$

Computing the magnitude of the electric field $\mathbf{E}_{0,ap}$ is a more involved process, and requires the wavefront curvature to be computed. This is the main development elaborated in [9], where the authors computed the propagating electric field in a single ODE, of which the derivation is not repeated here. Once the electric field magnitude is obtained, we can write the electric field at the aperture in complex form:

$$\mathbf{E}_{ap} = \mathbf{E}_{0,ap} e^{-jk_0\phi_{ap}} \tag{2.8}$$

Applying Schelkunoff's formulation of the surface equivalence theorem followed by the image theorem, we find the equivalent magnetic current at the aperture $\mathbf{M}_{ap}$, as shown in Equation 2.9.

$$\mathbf{M}_{ap} = 2\,\mathbf{E}_{ap} \times \hat{n} \tag{2.9}$$

The radiated far-field from this equivalent current can then be computed. This typically requires a Fourier transform of the equivalent currents (shown in Equation 2.10), which is computationally expensive. Furthermore, accurately computing the radiated far-field requires a large number of rays to obtain a fine distribution of the electric field, often including rays which do not go through the lens (spillover rays).

$$\mathbf{E}^{far} = -jk_0\eta \frac{e^{-jk_0 r}}{4\pi r} (\hat{\mathbf{I}} - \hat{\mathbf{r}}\hat{\mathbf{r}}) \cdot \iint_A \mathbf{M}(\mathbf{r}')\, e^{jk_0 \hat{\mathbf{r}}\cdot\mathbf{r}'}\, dA' \tag{2.10}$$

However, as was done by Budhu et al. in [17], it is possible to directly optimize for the equivalent current distribution, skipping the computationally expensive computation of the far-field radiation. This highlights an important trade-off; we can either have a detailed analysis of the inhomogeneous lens (including the radiated fields), for use in an optimization with a narrow solution space, or we can have a simplified analysis with a broader solution space. While both approaches are valid, we opt for the latter, as we know very little about the GRIN profile a priori.

2.3. Optimization of GRIN Lenses - 'The Inverse Problem'

Having outlined the chosen method to analyze GRIN lenses, we now turn our attention to the inverse problem. We first present a novel method to parametrize GRIN lenses, based on a Fourier series expansion of the refractive index. Then, we derive a fitness function based on a model for the desired field at the aperture. This function is minimized during the optimization, following a similar procedure as outlined in [17].

2.3.1. Parametrization of GRIN Lenses

For inputs to the optimization algorithm, we need some way to parametrize the refractive index distribution of a GRIN lens. As we first presented in [43], we propose to parametrize the refractive index using a Fourier series expansion, as shown in Equation 2.11. Here $\tilde{n}$

is the distribution of the refractive index, c_n are complex Fourier coefficients, and the vector $\mathbf{k}_n$ is the direction of the Fourier mode.

$$\tilde{n}(\mathbf{r}) = \mathrm{Re}\left(\sum c_n e^{j(\mathbf{k}_n \cdot \mathbf{r})}\right) \tag{2.11}$$

This distribution is then scaled to the achievable maximum and minimum refractive index n_{max} and n_{min}, as shown in Equation 2.12. This approach allows for a very wide search space, whilst guaranteeing that all possible solutions are within the achievable limits of the refractive index.

$$n(\mathbf{r}) = (\tilde{n}(\mathbf{r}) - \min(\tilde{n})) \cdot \frac{n_{max} - n_{min}}{\max(\tilde{n}) - \min(\tilde{n})} + n_{min}. \tag{2.12}$$

In the case of a flat lens with thickness t and side length l, we can formulate Equation 2.11 as Equation 2.13, where $[p, q, r]$ are the components of a given $\mathbf{k}_n$. This is visualized in Figure 2.8.

$$\tilde{n}(x, y, z) = \mathrm{Re}\left(\sum_{p,q,r} c_{p,q,r} e^{j\pi p \frac{x}{2l}} e^{j\pi q \frac{y}{2l}} e^{j\pi r \frac{z}{2t}}\right). \tag{2.13}$$

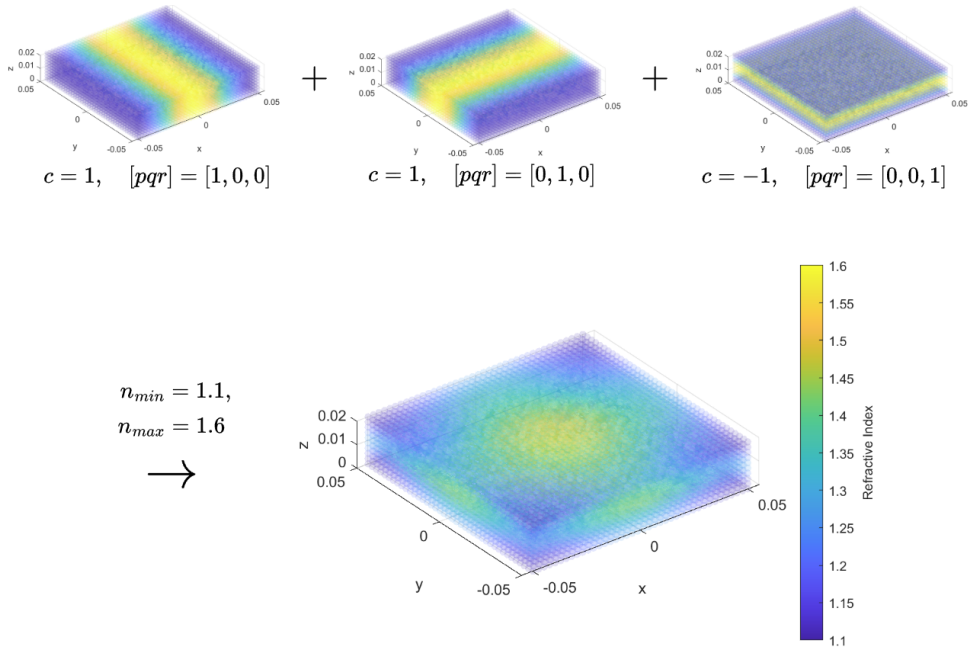

Figure 2.8: Vizualization of the parametrization of a flat GRIN lens, as described by Equation 2.13. The resulting distribution is the scaled to the maximum/minimum refractive index, as described by Equation 2.12.

This approach is particularly convenient for ray tracing, as we can easily compute the gradient of the refractive index. For Equation 2.13, we simply have

$$\nabla\tilde{n} = \mathrm{Re}\sum_{p,q,r}\left(\begin{bmatrix} jp\pi\frac{1}{2l}e^{jp\pi\frac{x}{2l}} \\ jq\pi\frac{1}{2l}e^{jq\pi\frac{x}{2l}} \\ jr\pi\frac{1}{2t}e^{jr\pi\frac{x}{2t}} \end{bmatrix} c_{p,q,r}e^{jp\pi\frac{x}{2l}}e^{jq\pi\frac{y}{2l}}e^{jr\pi\frac{z}{2t}}\right). \tag{2.14}$$

Applying the scaling of the minimum/maximum refractive index as described by Equation 2.12, we then arrive to Equation 2.15. Note that this is equivalent to multiplying each of the lens coefficients $c_{p,q,r}$ by a scalar.

$$\nabla n = \frac{n_{max} - n_{min}}{\max(\tilde{n}) - \min(\tilde{n})}\nabla\tilde{n}. \tag{2.15}$$

Though the derivation is not repeated here, the computation of the electric field shown in [9] requires the Hessian of the refractive index $\nabla\nabla n$. This can also be computed analytically, following similar steps as shown in Equation 2.14 and Equation 2.15 to obtain the 3x3 Hessian matrix.

2.3.2. Optimization

Our goal is to optimize for the Fourier coefficients. For this, we need to construct a an objective function, which is minimized when the solution is optimal. Following a similar approach as described in [17], we propose the following fitness function:[2]

$$\begin{aligned} \text{Fitness} = & 8\left(1 - \frac{1}{1+\sigma_\phi}\right) \\ & + 5\left(1 - \frac{1}{1+\sigma_{dir}}\right) \\ & + 3\left(1 - \frac{N_{rays,ap}}{N_{rays}}\right) \\ & + \left(\frac{V_{lens}}{V_{lens,max}}\right) \end{aligned} \tag{2.16}$$

The first term of Equation 2.16 is minimized when the phase at the aperture matches a given phase model, the second term is minimized when the ray direction matches the given model, the third term accounts for rays which are internally reflected or deviated away from the aperture, and the final term ensures the resulting lens is compact.

The weights of each term in Equation 2.16 were chosen by trial and error, starting with the values used in [17]. Some care must be taken not to weigh of the phase term too highly, as it becomes zero in the case that only one ray reaches the aperture (due to the standard deviation operator in Equation 2.21).

To increase the scan coverage of a given feed, we want the outgoing rays to be steered further away from the source. Let us define the target direction u_{target} and the 3x3 transfor-

[2]The terms 'objective function' and 'fitness function' seem to have varying definitions across different fields. Here, following the example set by Budhu et al. in [17], we use the term 'fitness function' for the function which is minimized during the optimization process.

mation matrix $[T]$ (see Figure 2.9). For the given case of a scan-enhancing lens in the xz plane, we could for example have

$$u_{target} = [T]\hat{s}^i \tag{2.17}$$

$$[T] = \begin{bmatrix} 2 & 0 & 0 \\ 0 & 0 & 0 \\ 0 & 0 & 1 \end{bmatrix} \tag{2.18}$$

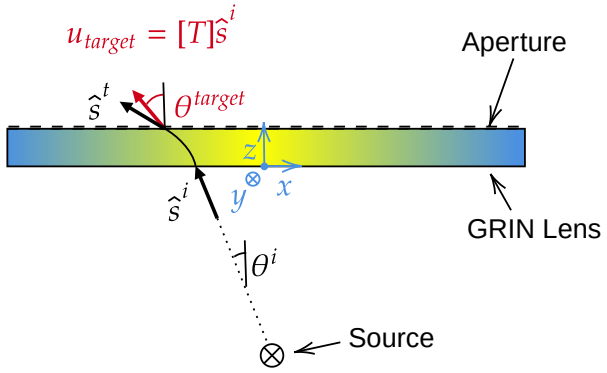

Figure 2.9: Diagram describing the transformation matrix $[T]$. The global coordinate system used in modeling the lens is shown in blue.

To visualize this, we can express this transformation as a mapping function between the angles θ^i and θ^{target} shown on Figure 2.9. With some simple trigonometry, we can derive the relation shown in Equation 2.19, plotted in Figure 2.10. We see that θ^{target} is initially double of θ^i, and tapers off as θ^i approaches $90°$. For example, an incident ray at $50°$ leads to an outgoing target ray of $67°$.

$$\theta^{target} = \arctan(2\tan(\theta^i)) \tag{2.19}$$

Normalizing the target direction to a unit vector $\hat{u}_{target}$, the terms σ_{dir} and σ_ϕ can in general be expressed as Equation 2.20, where the angled brackets indicate the average value of all $\hat{s}^t$. The phase model described by in Equation 2.21 is further discussed in Appendix C.

$$\sigma_{dir} = \langle|\hat{u}_{target} - \hat{s}^t|\rangle, \tag{2.20}$$

$$\sigma_\phi = \text{std}(\phi_{target} - \phi_{ap}), \quad \phi_{target} = k_0(\hat{u}_{target} \cdot \mathbf{r}_{ap}) \tag{2.21}$$

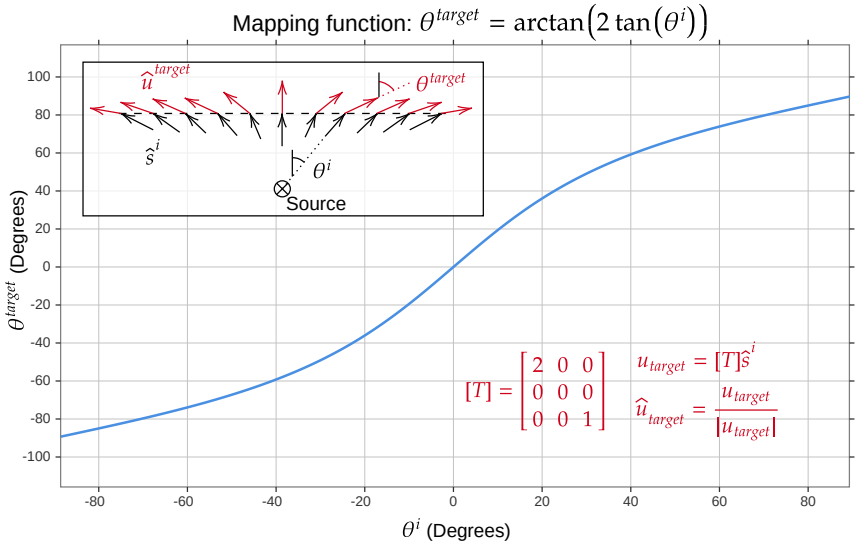

Figure 2.10: Visualization of the equivalent mapping function for the given transformation $[T]$ matrix.

An optimization algorithm is then used find the global minimum of the fitness function. A wide range of algorithms are available; here, we make use of the Particle Swarm Optimization (PSO) algorithm, a popular approach for problems in electromagnetics [18]. A key advantage of PSO is that few assumptions are made on the fitness function (and, in this case, we know very little about Equation 2.16 a priori).

Notably, this approach can be extended to a wide range of lenses; in fact, only the transformation matrix $[T]$ needs to be changed. For illustration, we consider the optimization of a simple collimating lens. In this case, $\hat{u}_{target}$ should be in the $\hat{z}$ direction, and the phase at the aperture should be uniform. This is equivalent to Equation 2.17 and Equation 2.20 with

$$[T] = \begin{bmatrix} 0 & 0 & 0 \\ 0 & 0 & 0 \\ 0 & 0 & 1 \end{bmatrix}. \tag{2.22}$$

Considering only the magnitude of two Fourier modes, we can visualize the fitness function on a 2D color chart, as shown in Figure 2.11. In a PSO optimization, several particles are created at random positions, and the fitness is evaluated at each particle. At each iteration, the particles move around the solution space, with their velocity influenced by the fitness of their neighbours, and the current best fitness of the swarm. This mimics the behaviour of bee swarms looking for flowers (as shown by the illustrations in [18]).

It is interesting to note the valley-like shape of the fitness function in Figure 2.11a. This is expected, as a result of the scaling refractive index described in Equation 2.12. Enforcing a constraint such as $||\mathbf{c}||_2 = 1$, where $\mathbf{c}$ is the vector containing all Fourier coefficients, would help reduce the optimization by one dimension. This is unfortunately not straightforward to implement with matlab's particleswarm solver.

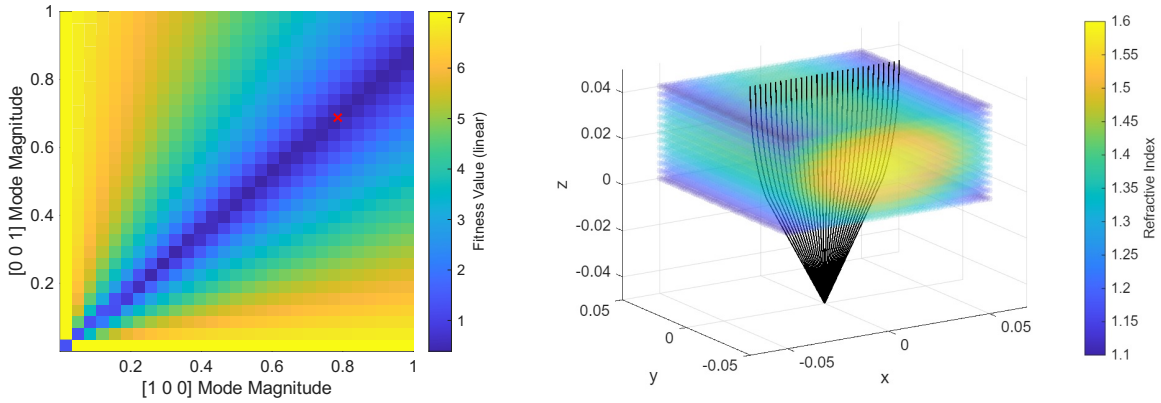

(a) Fitness function for a collimating lens with two modes, excluding the volume term. The red cross marks the optimal result found using a PSO algorithm.

(b) Raytracing through the optimal solution highlighted in Figure 2.11a.

Figure 2.11: Illustration of the optimization process for a collimating lens.

For the example shown in Figure 2.11, we consider only two inputs for the optimization (namely, the magnitude of the $[001]$ and $[100]$ modes). For the scan-enhancing lens, we take the following inputs:

- The maximum refractive index n_{max}
- The side length l
- The thickness l
- The magnitude of each mode
- The phase of each mode.

Selecting the mode directions included in the optimization is challenging, as each mode adds two inputs to the optimization, greatly expanding the search space. One must also be careful not to pick modes which are too large in magnitude; this translates to a rapid spatial variation of the refractive index, for which the curved-ray GO is not valid.

Here, we select 11 mode directions, shown in Table 3.1, which results in a total of 25 inputs to the optimization. Although this is difficult to visualize, the optimization procedure is essentially the same to the example shown in Figure 2.11.

3

Results & Measurements

3.1. 3D printing

To realize GRIN media using dielectric crystals, the unit cell must be small compared to the wavelength. There is a trade-off to be made here; a smaller unit cell size allows for higher frequency operation, at the cost of being more difficult to print & imposing a higher constraint on the minimum achievable volume fraction.

This trade-off was investigated by Wang et al. [44], who proposed that the unit cell size of gyroid dielectric crystals should be no larger than $1.4\lambda_g$, where the guide wavelength $\lambda_g = \lambda_0/\sqrt{\varepsilon_{eff}}$. Taking an operating frequency of $28\,\mathrm{GHz}$ ($\lambda_0 = 1.07\,\mathrm{cm}$) and a bulk permittivity of $\varepsilon_r = 2.6$, this gives a maximum unit cell size of $9.2\,\mathrm{mm}$. For margin, we choose to fix the unit cell size at $6\,\mathrm{mm}$; according to the results of Wang et al., this should allow for operation up to $43\,\mathrm{GHz}$ (though it is noted that this is not very conservative).

As discussed in section 2.1, gyroid surfaces can be represented by a simple trigonometric equation (Equation 3.1). Synthesizing a solid from this surface can be achieved using an inequality, as shown in Equation 3.2. This configuration is known as a sheet gyroid, where t is the half-thickness of the gyroid.

$$f(x, y, z) = \sin x \cos y + \sin y \cos z + \sin z \cos x, \tag{3.1}$$

$$|f(x, y, z)| \leq c \tag{3.2}$$

For use in Equation 2.2, we need the volume fraction δ of the gyroid. It is surprisingly difficult to relate c to δ; mathematically, this would be equivalent to Equation 3.3, where $\mathbf{1}\{\cdot\}$ is the indicator function. This integral cannot be solved analytically; in practice, the volume fraction of sheet gyroids is usually computed numerically, after the structure has been synthesized in a voxel grid.

$$\delta(c) = \frac{1}{(2\pi)^3} \iiint_0^{2\pi} \mathbf{1}\{f(x, y, z) \leq c\}\, dx\, dy\, dz, \quad 0 < c \leq 1.5 \tag{3.3}$$

To further complicate the matter, the realized volume fraction is dependent on the 3D printer extruder. Thus, it is best to relate δ to c using an empirical approach. To this end, 9 sets of cylindrical gyroid samples were printed using 3 different printers, after which their density was measured using calipers and a weighing scale. The resulting volume fraction is then computed using Equation 3.4, where ρ is the density of each sample. These results are shown in Figure 3.1.

$$\delta = \frac{\rho}{\text{mean}(\rho_{max})} \tag{3.4}$$

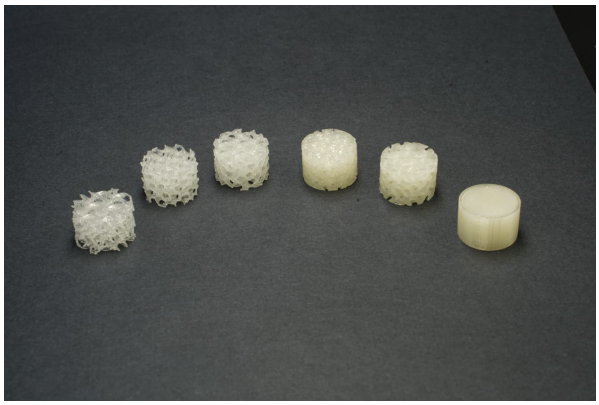

(a) Clear PLA cylindrical samples.

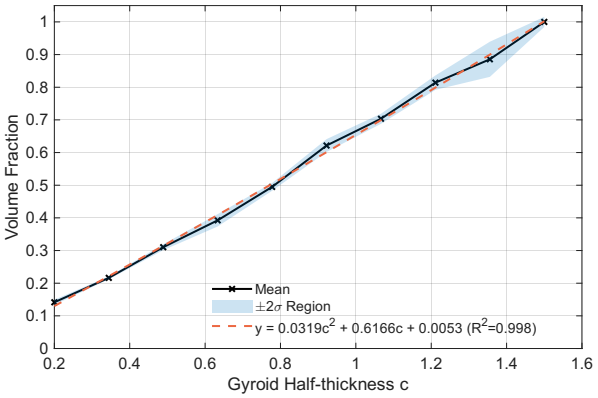

(b) Volume fraction of cylindrical sheet gyroid samples with a unit cell of $6\,\text{mm}$ (9 sets).

Figure 3.1: Volume fraction of 18x18x15 mm clear PLA cylindrical samples.

We observe a larger variance between samples at high volume fractions, with the $\pm 2\sigma$ region spanning around $10\,\%$ of the volume fraction. At these high infill percentages, much of the volume is filled with 100% rectilinear infill pattern, which is known to vary between different extruders in FFF printers [45]. This can be easily verified by separating the results for different printers (Figure 3.2), where we have excellent repeatability ($\pm 2\sigma$ region spanning $<1\,\%$).

A full design of experiments investigation is outside the scope of this work; the aim of this data is to quantify the error which may arise from the 3D printing process. Here, we use the least squares regression corresponding to the first Prusa Mk4 printer, which was used for the remainder of this thesis.

3.2. Permittivity Measurements of PLA

For use in the Maxwell Garnett relation (Equation 2.2), we need the value of permittivity of bulk PLA. This data has been reported in literature, for example in [41]. Nevertheless, it is interesting to take permittivity measurements with our selected filament and printer.

There are a range of techniques available for permittivity measurements at microwave frequencies, as described in [46]. A test setup based on the dielectric probe method was available in Delft, shown in Figure 3.3a. Measurements were attempted with this setup, but the results are unfortunately rather poor. In particular, the S11 parameter (shown in Figure 3.3b) exceeds 1 at some frequencies. This should be physically impossible, and suggests an issue with the setup or calibration.

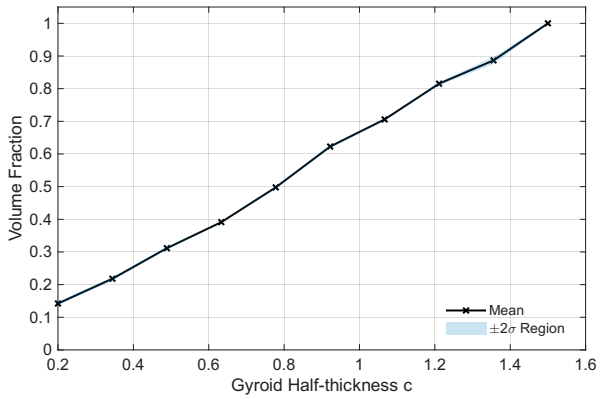

(a) Samples printed on Prusa Mk4 #1 (3 sets)

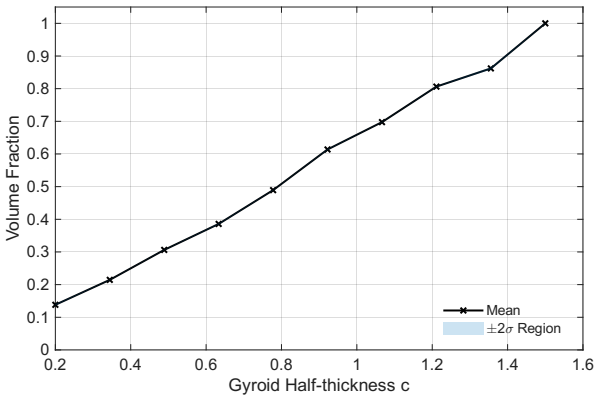

(b) Samples printed on Prusa Mk4 #2 (3 sets)

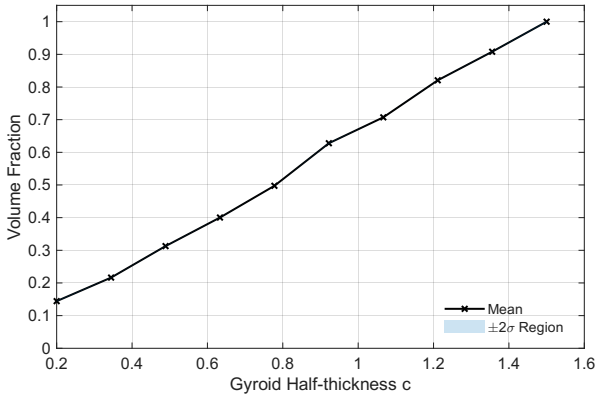

(c) Samples printed on Prusa XL (3 sets)

Figure 3.2: Volume fraction of cylindrical samples, separated by the printer used.

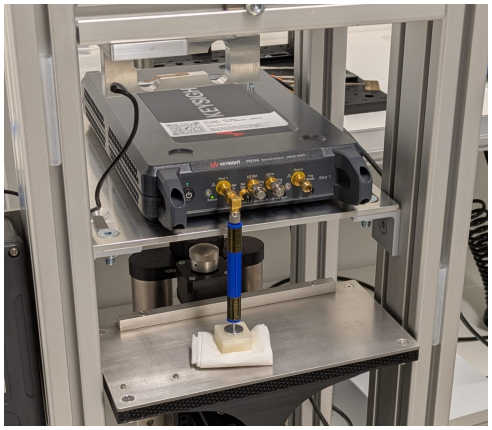

(a) Measurement of a clear PLA sample with a dielectric probe.

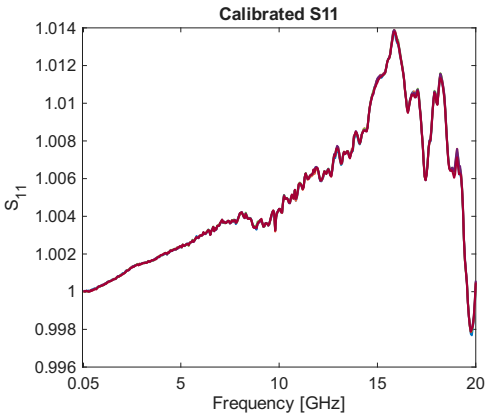

(b) S11 parameters (calibrated) obtained from the measurements with the dielectric probe.

Figure 3.3: Results of the dielectric probe measurements

Although we are grateful to Tim Hosman for his help with these measurements, the data obtained was unfortunately unsuitable, and it should be noted that dielectric probe setups are not well suited to low-loss materials.

For high precision measurements of low-loss polymers, resonator methods are best suited. Clear PLA samples were measured by the IT'IS Foundation using a DAK-R split cylinder res-

onator. This approach produced excellent results, showing close agreement with literature [41]. The permittivity and loss tangent are presented in Figure 3.4.

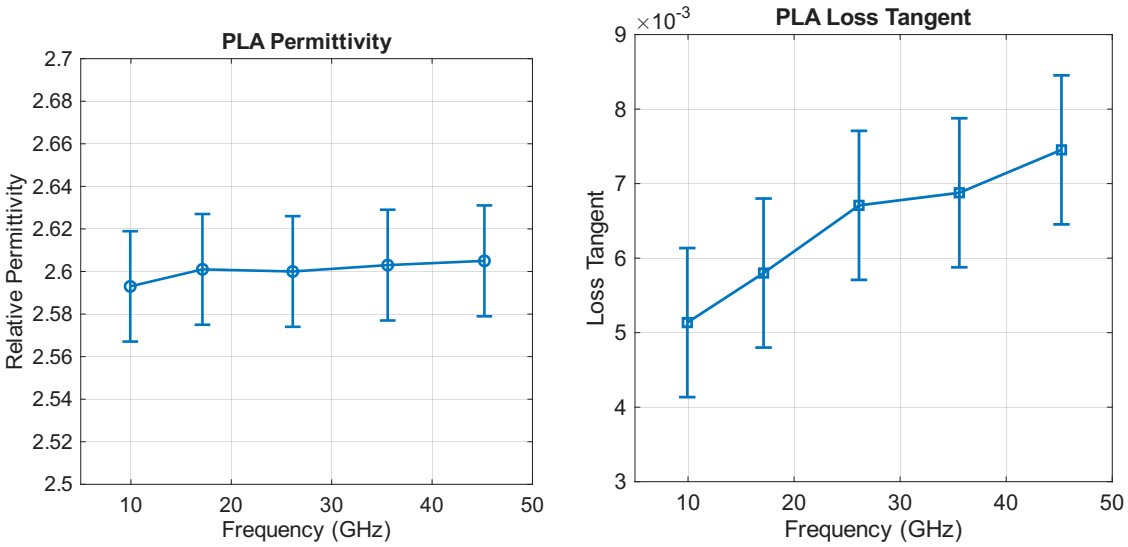

(a) Permittivity of clear PLA measured with the DAK-R split cylinder resonator.

(b) Loss tangent of clear PLA measured with the DAK-R split cylinder resonator.

Figure 3.4: Complex permittivity measurements of clear PLA measured with the DAK-R split cylinder resonator (performed by IT'IS).

3.3. Validation Case: Optimization of a Luneburg Lens

The well-known Luneburg lens provides is convenient to validate the optimization procedure. Using the Fourier series parametrization method described in subsection 2.3.1, we can define the GRIN profile of a spherically symmetric lens as Equation 3.5.

$$\tilde{n}(r) = \mathrm{Re}\left(\sum c_p e^{j\pi p \frac{r}{2R}}\right) \tag{3.5}$$

By setting the minimum refractive index to $n_{min} = 1$, we can then use a PSO algorithm and compare the results with the ideal Luneburg lens GRIN profile (as defined by Equation 1.1). The optimizer recovers a solution close to the ideal Luneburg lens profile, as shown in Figure 3.5. Furthermore, we see that the fitness of the Luneburg lens is very close to zero, validating the ray-tracing algorithm and the fitness function for use in an ideal lens.

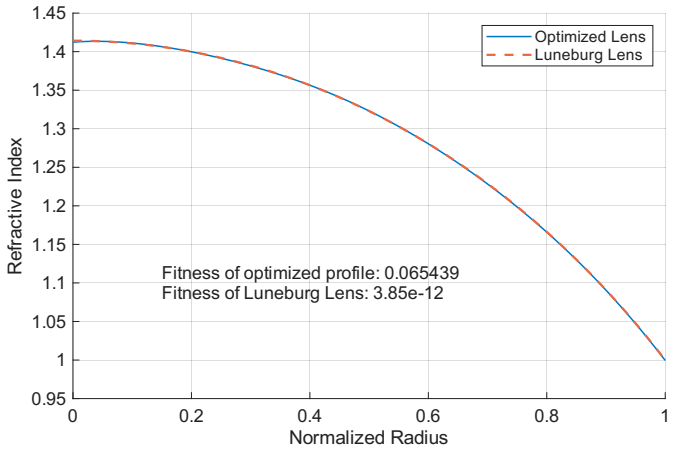

(a) Results of the optimization of a Luneburg-like lens with 6 Fourier modes.

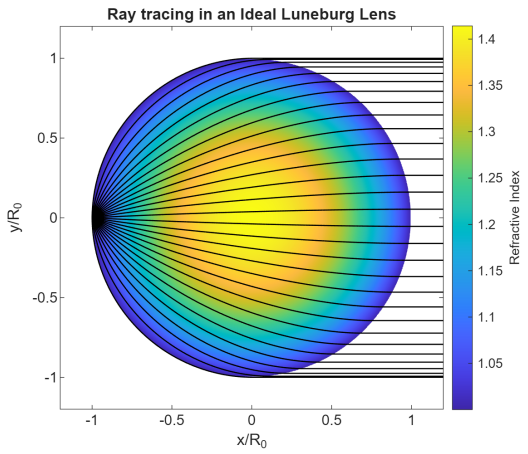

(b) Ray-tracing in an ideal Luneburg lens.

Figure 3.5: Validation of the ray-tracing code and optimization algorithm with the Luneburg lens, as defined by Equation 1.1.

In the ideal Luneburg lens, the refractive index approaches 1 at the edge of the lens. However, this cannot be realized in practice, as there is a lower limit on the achievable refractive index imposed by the minimum wall thickness. Using the method presented in this thesis, we can optimize a spherical lens accounting for these manufacturing limits.

Running the optimizer again with $n_{min} = 1.1$, we find a marginally improved solution over the ideal Luneburg lens profile truncated to the lower limit, as shown in Figure 3.6.

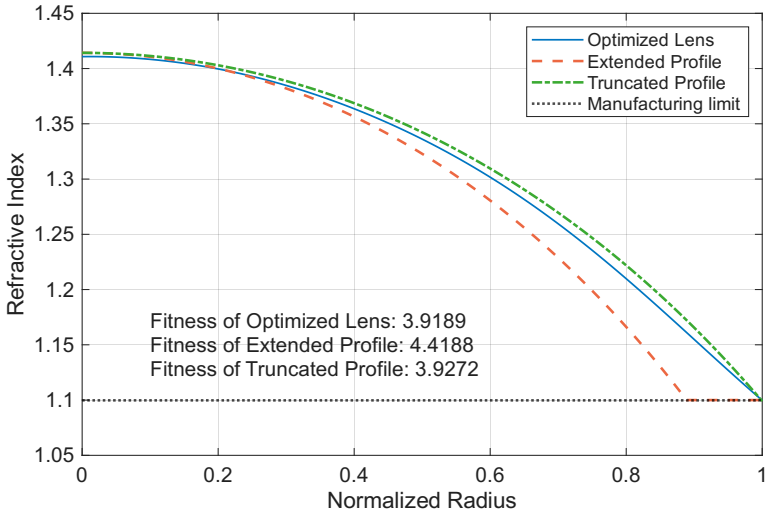

Figure 3.6: Comparison of the GRIN profiles of the optimized and ideal Luneburg lens, with the constraint of $n_{min} = 1.1$.

A well-known application of Luneburg lenses is as a Radar Cross-Section (RCS) reflector; By partially covering the lens with a metalized cap, a wide-angle RCS reflector can be realized. The optimized lens was printed, fitted with a metalized cap, and the RCS was measured in the DUCAT facility. Further details are provided in [43].

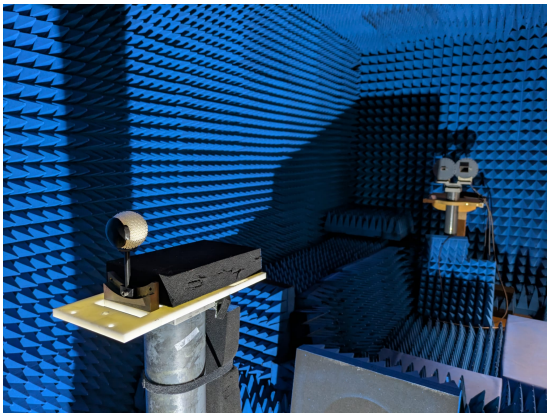

(a) Test setup for RCS measurements in DUCAT.

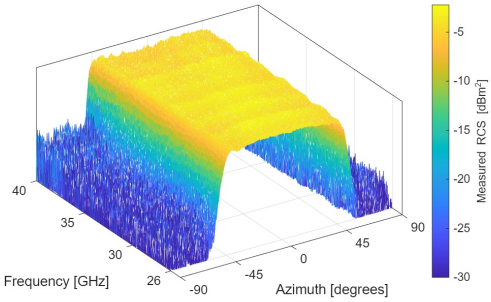

(b) RCS of the optimized Luneburg lens reflector over azimuth and frequency.

Figure 3.7: RCS measurements of the optimized Luneburg lens reflector.

3.4. Optimization of a Scan-Enhancing Flat GRIN Lens

The PSO approach outlined in section 2.3 was implemented using the particleswarm solver in Matlab's global optimization toolbox. The optimization was run for 500 iterations, with a swarm size of 300 particles.

The source used in the optimization is shown in Figure 3.8, featuring 3 rows of 30 rays, uniformedly spaced at the aperture. The rays have a beamwidth of $120°$ in the xz place, and of $15°$ in the yz plane. These values were chosen somewhat arbitrarily, and similar lenses were obtained with a range of different sources. With this source, propagating 90 GO rays and evaluating the fitness function takes approximately $1.8\,\mathrm{s}$, running on a low-powered machine. The total time for the optimization was approximately 60 hours; this could be greatly reduced by running the optimization on more powerful machines, and by further reducing the number of GO rays.

The selected Fourier mode directions $[pqr]$ are mostly in the xz plane, with only one mode ($[010]$) being in the yz plane (intended to provide some collimation in the yz plane). It should also be noted that the mode directions does not necessarily need to be an integer. In fact, one could even use the values of $[pqr]$ as optimization variables. Although this is mathematically sound, it was found not to offer meaningful advantages, and is more difficult to visualize.

The results of the optimization are shown in Table 3.1, where $c_{[pqr]}$ is the complex coefficient for the given Fourier mode direction $[pqr]$, as shown in Equation 3.6. The optimized flat lens is shown in Figure 3.8.

$$\tilde{n}(x,y,z) = \mathrm{Re}\left(\sum c_{[pqr]} e^{j\pi(p\frac{x}{2l}+q\frac{y}{2l}+r\frac{z}{2t})}\right) \tag{3.6}$$

To validate the performance of the scan enhancing lens, we test it using the TMYTEK BBox 5G development beamformer. A support structure was printed to support the lens $4.5\,\mathrm{cm}$ from the array (the blue structure seen in Figure 3.9b). We expect this structure to have minimal effect on the radiation patter; to verify this, the radiation pattern of the array steered to broadside was measured with and without the structure, shown in Figure 3.11a. We

Table 3.1: Optimization result of the PSO algorithm for the flat scan enhancing lens, for use with Equation 3.6. Readers should note that the overline indicates a negative number.

Parameter	Lower Bound (Magnitude/Phase)	Upper Bound (Magnitude/Phase)	Magnitude	Phase (rad)
$n_{\max}$	1.15	1.60	1.6000	-
l	0.10	0.20	0.2000	-
t	0.01	0.05	0.0242	-
$c_{[001]}$	$0/0$	$1/2\pi$	0.4657	-1.4527
$c_{[002]}$	$0/0$	$1/2\pi$	0.2666	0.6133
$c_{[003]}$	$0/0$	$1/2\pi$	0.0719	2.6927
$c_{[100]}$	$0/0$	$1/2\pi$	0.8470	0.0007
$c_{[200]}$	$0/0$	$1/2\pi$	0.9181	-0.0301
$c_{[300]}$	$0/0$	$1/2\pi$	0.8308	3.1294
$c_{[101]}$	$0/0$	$1/2\pi$	0.0227	0.6964
$c_{[\bar{1}01]}$	$0/0$	$1/2\pi$	0.0516	-0.1319
$c_{[201]}$	$0/0$	$1/2\pi$	0.0413	-0.0369
$c_{[\bar{2}01]}$	$0/0$	$1/2\pi$	0.0144	-0.3419
$c_{[010]}$	$0/0$	$1/2\pi$	0.6692	-0.0000

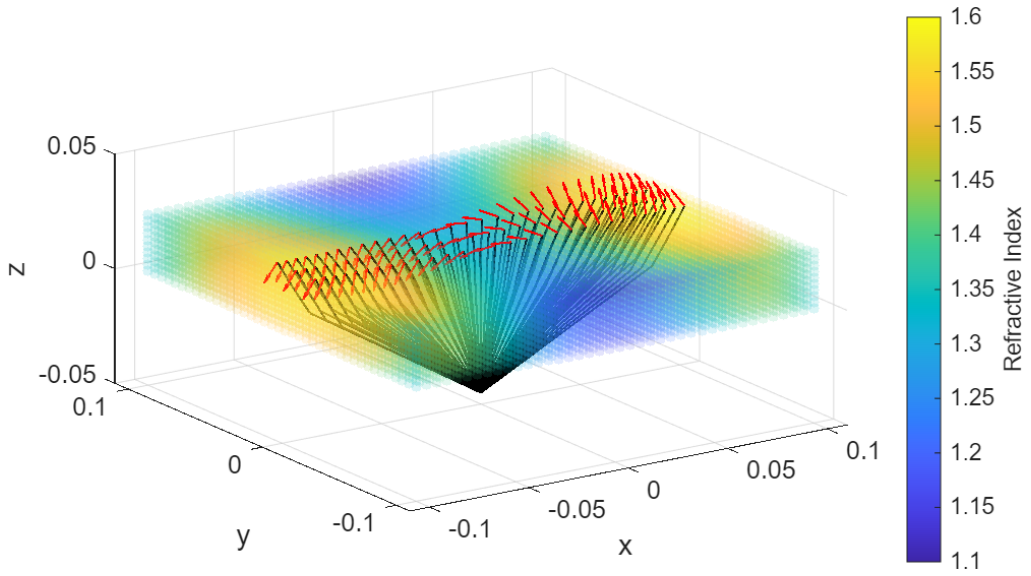

Figure 3.8: Ray tracing through the optimized scan-enhancing lens, with the 30x3 source used in the optimization. The red vectors represent the electric field at the aperture.

see that the radiation pattern of the BBox in clean configuration (i.e. without the support structure) is near identical to the pattern with only the support structure.

The test setup is outlined in Figure 3.9a; in this case, the S21 parameter is measured, using the BBox in reception.

As a baseline, we first take antenna pattern measurements without the lens. We note that

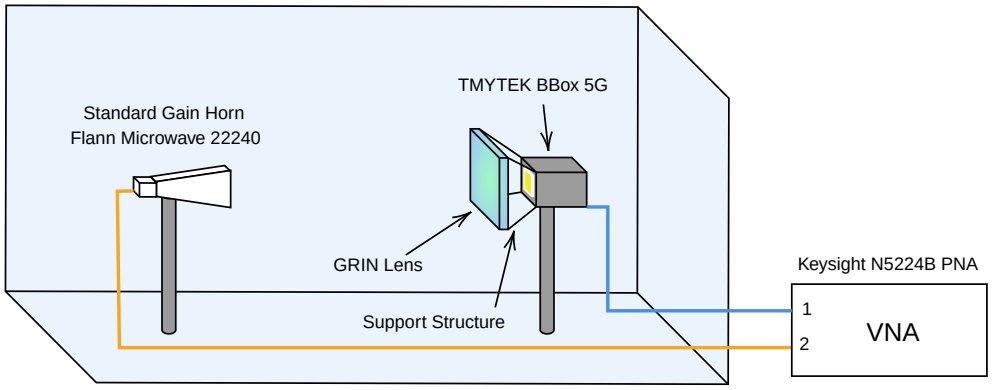

(a) Diagram of the measurement scheme.

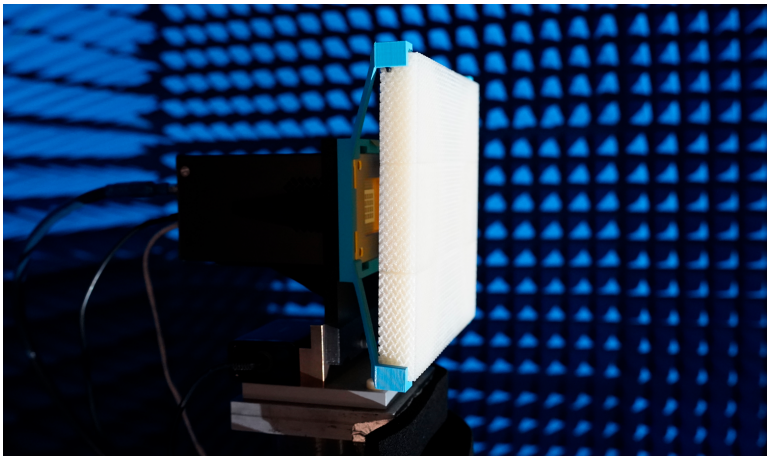

(b) Scan enhancing lens fitted onto the TMYTEK BBox 5G beamformer in DUCAT.

Figure 3.9: Measurement scheme for the scan enhancing GRIN lens in DUCAT.

a grating lobe begins appears when steering beyond $45°$ away from broadside, as seem in Figure 3.10a.

Taking a closer look, we see in Figure 3.11a that the lens broadens the main lobe when the array is steered to broadside. This is expected, considering the selected transformation matrix defined in Equation 2.18. We also overlay the array factor for a 4x4 array of isotropic elements with half-wavelength spacing, where we see a good match for the beamwidth and sidelobe location.

Looking at Figure 3.11b, we see that the array with the lens offers significantly improved performance compared to the array in free space steered at $50°$, with an increase in gain of approximately $6\,\mathrm{dB}$. A strong grating lobe is present at $-25°$ when the array is steered to $50°$; it should be noted that this is outside the advertised scan range of the BBox, and the phase of each element was manually adjusted to obtain this pattern.

Overlaying the results in Figure 3.12, we see that the scan envelope is increased by approx-

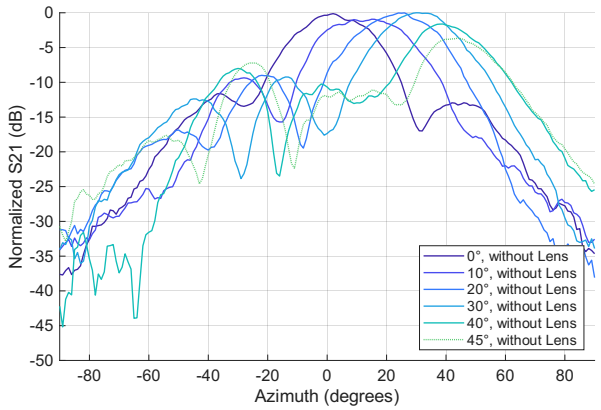

(a) BBox antenna pattern measurements without the lens (baseline) Note the appearance of a grating lobe at $-25°$ of azimuth when the beam is steered to $45°$.

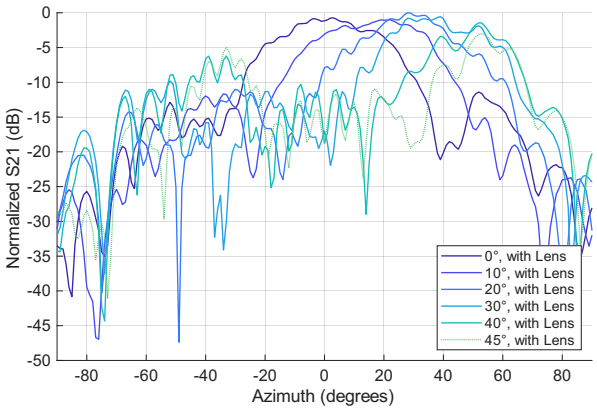

(b) BBox antenna pattern measurements with the lens.

Figure 3.10: BBox Antenna pattern measurements, with and without the scan-enhancing lens.

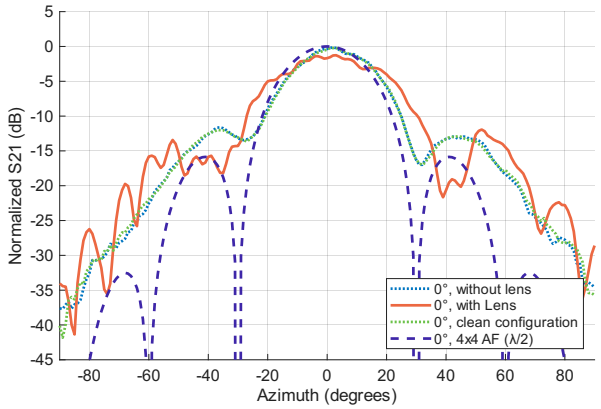

(a) BBox antenna patterns at broadside with and without the scan-enhancing lens, normalized to the same scale. The pattern without the support structure is also shown, along with the array factor for an array of isotropic elements with half-wavelength spacing.

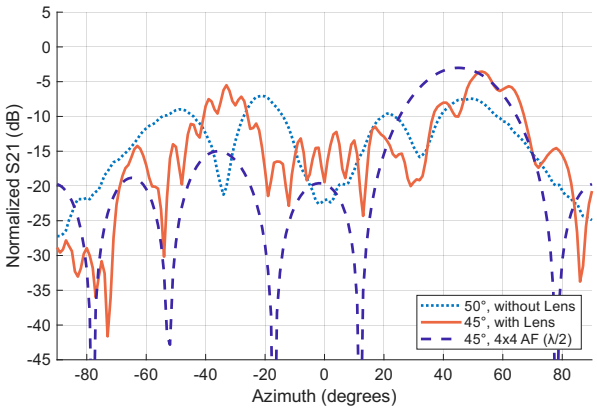

(b) Comparison of the array steered to $50°$ without the lens, and the array steered to $45°$ with the scan-enhancing lens, normalized to the same scale. The Array Factor includes a scan loss term of $\cos(\theta)$.

Figure 3.11: BBox Antenna pattern measurements, with and without the scan-enhancing lens.

imately $10°$ (or a total of $20°$, assuming that the pattern would be symmetric for negative values of azimuth). This improvement, along with the broadening of the main lobe beamwidth by $\sim 10°$, are consistent with the function shown in Figure 2.10.

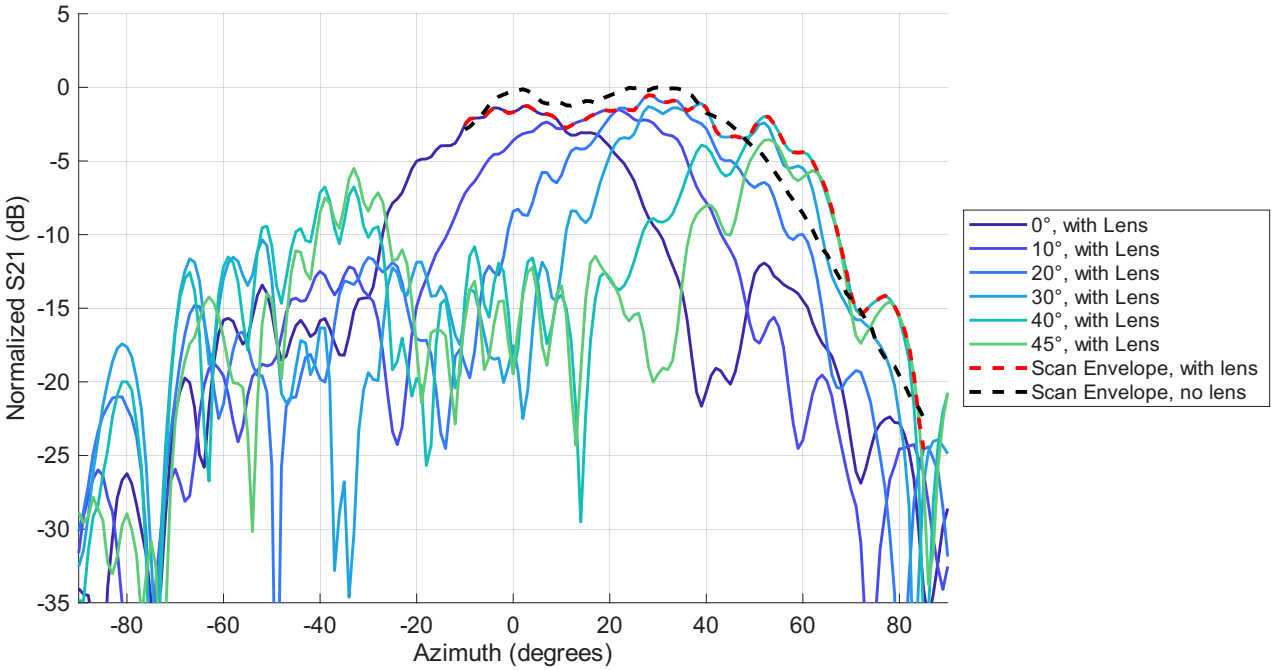

Figure 3.12: Comparison of the scan envelopes (i.e. the max gain of each pattern, taken at 10° intervals), normalized to the same scale. The patterns of the array with the scan-enhancing lens are overlaid.

4

Conclusions

4.1. Conclusions

Using a novel technique to parametrize the GRIN profiles, we have presented a method to systematically design, optimize and fabricate GRIN lenses to enhance phased array antennas. This parametrization allows for a very wide search space, enabling the design of GRIN lenses without making initial assumptions on the refractive index profile. As an improvement over the 2D spline parametrization used in [17], this approach also directly accounts for the limits of the refractive index imposed by the manufacturing process.

This approach is experimentally validated with the optimization of a flat GRIN lens which increases the scan envelope of a TMYTEK BBox 5G 28GHz phased array antenna by ± 10 degrees, demonstrating the possibility of drop-in improvements to phased array antennas with GRIN lenses.

We now revisit the research questions discussed in subsection 1.3.2;

RQ1.1: Which computational tools are best suited to synthesize air-dielectric GRIN media for use at microwave frequencies?

Graded Triply Periodic Minimal Surface (TPMS) are a powerful tool to synthesize GRIN media based on dielectric crystals at microwave frequencies; they offer a continuously varying density gradient compared to the typical approach of parametrized unit cells, and are significantly less computationally expensive than the Spatially Variant Lattice (SVL) algorithm.

RQ1.2: How can FFF filaments be selected and characterized for use in GRIN lenses at microwave frequencies?

A critical factor when selecting materials for use in GRIN lenses is the dielectric loss, as illustrated by Figure 2.4 and Figure 2.5. While PLA offers acceptable performance for a demonstrator, it would not be suited to a real system, or for use at higher frequencies. Permittivity measurements of the filament used in this work were performed by IT'IS, as reported in Figure 3.4. It is noted that taking permittivity measurements at microwave frequencies is challenging, and requires an appropriate test setup.

RQ1.3: How do manufacturing constraints arising from the FFF process impact the design

of gradient index lenses?

Due to the minimum realizable wall thickness of FFF printing, there is a lower limit on the ε_{eff} which can be realized. This effect is especially pronounced when using a small unit cell, or when using materials with a high bulk permittivity. The parametrization illustrated in Figure 2.8 allows for the synthesis of GRIN profiles which are always within the achievable range of refractive index.

RQ2.1: Which computational electromagnetics methods are suited to the analysis of GRIN lenses in optimization workflows?

There is an important trade-off to be made here; using a more detailed analysis method could allow for the optimization of more complex objectives, such as maximizing radiation efficiency, enforcing a certain sidelobe level, or arbitrary pattern shaping. However, the increased computational cost would require a more constrained solution space. The approach presented here (optimizing directly for the electric field at the aperture) allows for a very wide solution space, which is helpful for multi-objective optimizations, or when an initial guess for the GRIN profile of the lens is not available.

RQ2.2: Which simplifying assumptions can be made without significantly degrading accuracy when analyzing the effect of GRIN lenses on phased array antennas?

As elaborated in Appendix B, the key assumption in Geometrical Optics is that the wavelength is vanishingly small. Interestingly, we see that GO can still be used to optimize microwave lenses at the scale presented here, where the lens is only a few wavelengths thick. One key assumption of our modeling approach is the representation of the phased array as a point source; this is only valid because the lens is in the far-field of the array, which would be impractical for a large array antenna. Our approach could be extended to large arrays by summing the electric field at the aperture for each individual element. Lastly, we assume that the dielectric crystal behaves as though it was a homogeneous medium, following the Maxwell Garnett approximation. From the RCS measurements of the Luneburg lens, we see that our dielectric crystals with a unit cell size of $6\,\mathrm{mm}$ are effective up to frequencies around $35\,\mathrm{GHz}$.

Overall, the flat scan-enhancing GRIN lens offers modest improvements to the scanning performance of a given phased array antenna, comparable to existing dielectric dome lenses. The given constraints of a flat lens in the far field of the antenna pose a challenge, requiring a relatively large lens to capture the radiation of the array. Nevertheless, the flat lens demonstrates the freedom in the form factor afforded by GRIN lenses.

Two publications were derived from the work in this thesis:

- A conference paper on the optimization of the Luneburg lens (see section 3.3) was submitted to the 20$^{\text{th}}$ European Conference on Antennas and Propagation, titled ”Fourier Series-Based Optimization of Gradient Index Lens Permittivity Profiles Within Manufacturing Limits” [43] **(accepted)**.
- At the time of writing this thesis, a paper is being prepared for submission to the IEEE Antennas and Wireless Propagation Letters Special Cluster ”Dielectric antennas from the microwave to the terahertz range, and beyond” **(in preparation)**.

4.2. Recommendations for Future Work

Building on the framework developed in this thesis, a number of recommendations are made for further research on the design and fabrication of GRIN lenses.

A key novel development presented this work is the parametrization of GRIN media as a Fourier series expansion. A number of recommendations are proposed on this topic;

- This parametrization could be beneficial for the design of other GRIN components, such as inhomogeneous Dielectric Resonator Antennas (DRA)s and waveguide filters. This could be done using similar multi-objective optimization algorithms as this thesis, or for use in analytical models.
- It was found that this parametrization permits the optimization using a small number of GO rays, greatly reducing the computational effort compared to PO methods. In this case, the number of rays was chosen arbitrarily. A systematic study on the convergence of such optimizations with fewer rays would be beneficial.
- In this study, we impose no constraints on the coefficients of the Fourier series, allowing for any combination of modes. By imposing a limit on the magnitude of each mode, one could enforce a certain smoothness on the refractive index distribution. To give a concrete example, a decay rate on the coefficients proportional to $1/|\mathbf{k}_n|^4$ would result in a continuous second derivative of the refractive index, regardless of the number of modes. This could be used to enforce a slowly varying GRIN profile, which is necessary for the curved-ray GO assumption to hold.

Here, we employed an optimization algorithm very similar to the one presented by Budhu et al. in 2019 [17]. There have been considerable developments in multi-objective optimization since, which would be interesting for the use case presented here;

- As discussed in **RQ2.1** in section 4.1, there is a trade-off to be made between the detail in the analysis of GRIN lenses, and the search space for the optimization. Here, we have opted for a very large search space with a highly simplified analysis. It would be interesting to investigate the reverse; one could run a small number (>100) of full-wave simulations, and make use of surrogate optimization algorithms & machine learning to design GRIN lenses within a more constrained search space.
- Here, we limit the investigation to a scan-enhancing lens in a single cut plane. The optimization procedure described in this thesis should be directly applicable to a 2D case, only modifying the matrix $[T]$ and the input mode directions. In a similar vein, this work could be extended to design a non-flat GRIN lens; notably, a dome-like lens would likely be more compact and offer better performance beyond $60°$.

Besides this, a number of ongoing developments in additive manufacturing would be of interest for microwave GRIN lenses;

- Here, we made use of PLA filament, due to its low cost and good printability. Much better performance could be obtained with low loss materials, such as 3D printed sintered ceramics (see Figure 2.4). It is also possible to print birefringent materials such as Liquid Crystal Polymer (LCP), allowing for the design of tailored anisotropic GRIN profiles.

- Beyond TPMS structures, one particularly interesting class of functionally graded structures are spinodoids; these are stochastically generated structures where the density and anisotropy can be locally controlled. This allows for the synthesis dielectric crystals with controlled anisotropy, and the stochastic nature of these structures may help extend the usable frequency range of GRIN lenses.
- Interestingly, a limiting factor in this work was the slicer. The printed structures featured in this thesis were synthesized using LisbonTPMS, after which the mesh was sliced using PrusaSlicer. For the flat lens shown in Figure 3.9b, the slicing process took several hours (and would not permit thicker lenses). Furthermore, all edges are treated as perimeters in the slicer, resulting in very long print times for TPMS structures with low volume fractions (in the order of weeks). A tool to synthesize efficient toolpaths to print arbitrarily graded structures would be greatly beneficial.

References

[1] G. Federico, D. Caratelli, G. Theis, and A. B. Smolders. “A Review of Antenna Array Technologies for Point-to-Point and Point-to-Multipoint Wireless Communications at Millimeter-Wave Frequencies”. In: *International Journal of Antennas and Propagation* 1 (2021). DOI: 10.1155/2021/5559765.

[2] Constantine A. Balanis. *Antenna Theory: Analysis and Design*. Wiley, 1996. ISBN: 978-0-471-59268-6.

[3] Hui Chu, Chuan Shao, Xiaohua Zhu, and Yong-Xin Guo. “Design of a phased array antenna with scan loss reduction and gain enhancement by using reconfigurable sub-arrays”. In: *IET Microwaves, Antennas & Propagation* 13 (2022). DOI: 10.1049/mia2.12276.

[4] Lars Josefsson and Patrik Persson. *Conformal Array Antenna Theory and Design*. John Wiley & Sons, 2006. ISBN: 978-0-471-46584-3.

[5] Yipeng Wang et al. “Grating-Lobe Reduction for Uniform Undersampled Phased Array Using Dielectric Dome Lens”. In: *IEEE Transactions on Antennas and Propagation* 3 (2025). DOI: 10.1109/TAP.2024.3508103.

[6] Irina Munina, Igor Grigoriev, Garret O’donnell, and Daniel Trimble. “A Review of 3D Printed Gradient Refractive Index Lens Antennas”. In: *IEEE Access* (2023). DOI: 10.1109/ACCESS.2023.3239782.

[7] R. K. Luneburg and M. Herzberger. *Mathematical Theory of Optics*. 1st ed. University of California Press, 1964. ISBN: 978-0-520-36850-7. DOI: 10.2307/jj.8501483.

[8] Jagadis Chunder Bose. “I. On the determination of the indices of refraction of various substances for the electric ray. I. Index of refraction of sulphur”. In: *Proceedings of the Royal Society of London* 353-358 (1896). DOI: 10.1098/rspl.1895.0069.

[9] Ilir Gashi, Anastasios Paraskevopoulos, Stefano Maci, and Matteo Albani. “GO Analysis of GRIN Lens Antennas by Combining in a Single ODE, Field and Wavefront-Curvature Transport to the Ray Tracing”. In: *IEEE Transactions on Antennas and Propagation* 3 (2024). DOI: 10.1109/TAP.2024.3360727.

[10] Modeste Bodehou, David González-Ovejero, Christophe Craeye, and Isabelle Huynen. “Method of Moments Simulation of Modulated Metasurface Antennas With a Set of Orthogonal Entire-Domain Basis Functions”. In: *IEEE Transactions on Antennas and Propagation* 2 (2019). DOI: 10.1109/TAP.2018.2880075.

[11] Thomas Binzer, Michael Klar, and Volker Gross. “Development of 77 GHz Radar Lens Antennas for Automotive Applications Based on Given Requirements”. In: *2007 2nd International ITG Conference on Antennas*. 2007. DOI: 10.1109/INICA.2007.4353963.

[12] M. Kamran Saleem, Hamsakutty Vettikaladi, Majeed A. S. Alkanhal, and Mohamed Himdi. “Lens Antenna for Wide Angle Beam Scanning at 79 GHz for Automotive Short Range Radar Applications”. In: *IEEE Transactions on Antennas and Propagation* 4 (2017). DOI: 10.1109/TAP.2017.2669726.

[13] H. Zhang. “Analysis and Design of Lens Antenna Systems for Applications at Millimeter and Sub-millimeter Wavelengths”. PhD thesis. Delft University of Technology, 2024. DOI: 10.4233/UUID:5FB0DFE6-94CC-40F1-8773-91367B5E2FBA.

[14] J. B. Pendry, D. Schurig, and D. R. Smith. “Controlling Electromagnetic Fields”. In: *Science* 5781 (2006). DOI: 10.1126/science.1125907.

[15] Xuanjing Li et al. “Additively-Manufactured Broadband Metamaterial-Based Luneburg Lens for Flexible Beam Scanning”. In: *Materials* 12 (2024). DOI: 10.3390/ma17122847.

[16] Mahsa Ebrahimpouri and Oscar Quevedo-Teruel. “Bespoke Lenses Based on Quasi-Conformal Transformation Optics Technique”. In: *IEEE Transactions on Antennas and Propagation* 5 (2017). DOI: 10.1109/TAP.2017.2679494.

[17] Jordan Budhu and Yahya Rahmat-Samii. “A Novel and Systematic Approach to Inhomogeneous Dielectric Lens Design Based on Curved Ray Geometrical Optics and Particle Swarm Optimization”. In: *IEEE Transactions on Antennas and Propagation* 6 (2019). DOI: 10.1109/TAP.2019.2902737.

[18] J. Robinson and Y. Rahmat-Samii. “Particle swarm optimization in electromagnetics”. In: *IEEE Transactions on Antennas and Propagation* 2 (2004). DOI: 10.1109/TAP.2004.823969.

[19] Jingwei Xu et al. “Multiobjective Optimization of Bespoke Gradient-Index Lenses: A Powerful Tool for Overcoming the Limitations of Transformation Optics”. In: *Physical Review Applied* 2 (2022). DOI: 10.1103/PhysRevApplied.18.024021.

[20] Nicolas Garcia and Jonathan Chisum. “Reduced dimensionality optimizer for efficient design of wideband millimeter-wave 3D metamaterial GRIN lenses”. In: *Microwave and Optical Technology Letters* 5 (2021). DOI: 10.1002/mop.32755.

[21] Pilar Castillo-Tapia, Núria Flores-Espinosa, Francisco Mesa, Maria Carolina Viganó, and Oscar Quevedo-Teruel. “Improving the Scanning Coverage of Array Antennas With Multilayer Lenses Designed With a Ray Tracing”. In: *IEEE Antennas and Wireless Propagation Letters* 3 (2025). DOI: 10.1109/LAWP.2024.3507178.

[22] Zhishu Qu, Shi-Wei Qu, Zhe Zhang, Shiwen Yang, and Chi Hou Chan. “Wide-Angle Scanning Lens Fed by Small-Scale Antenna Array for 5G in Millimeter-Wave Band”. In: *IEEE Transactions on Antennas and Propagation* 5 (2020). DOI: 10.1109/TAP.2020.2967086.

[23] Giselle Hsiang Loh, Eujin Pei, David Harrison, and Mario D. Monzón. “An overview of functionally graded additive manufacturing”. In: *Additive Manufacturing* (2018). DOI: 10.1016/j.addma.2018.06.023.

[24] Bradley P. DUNCAN, Maxwell E. PLAUT, Theodore H. Fedynyshyn, and Jennifer A. Lewis. “3-d printed devices formed with conductive inks and method of making”. US20190300741A1. 2019.

[25] Gautier Mazingue, Benedikt Byrne, Maxime Romier, and Nicolas Capet. “3D Printed Ceramic Antennas for Space Applications”. In: *2020 14th European Conference on Antennas and Propagation (EuCAP)*. 2020. DOI: 10.23919/EuCAP48036.2020.9135312.

[26] Wuzhao Li, Siqian Wu, Jin Chen, Rong Wang, and Qi Ge. “Digital light processing 3D printing of ceramics for W-band gradient refractive index metalens”. In: *International Journal of Extreme Manufacturing* 1 (2025). DOI: 10.1088/2631-7990/ae0b0d.

[27] Simon Hehenberger. “Homogenization and Characterization of Additive Manufactured Dielectric Crystals for High-Frequency Electromagnetic Applications”. PhD thesis. 2025.

[28] Hairu Wang et al. “6G energy-efficient systems based on arrays combined with dielectric lenses”. In: *Electronics Letters* 17 (2023). DOI: 10.1049/ell2.12932.

[29] Ebenezer Tawiah Ashong, Van Thang Nguyen, and Jae-Young Chung. “Angular Scan Enhancement of Ka-Band Circularly Polarized Phased Array Using Dielectric Dome”. In: *IEEE Access* (2024). DOI: 10.1109/ACCESS.2024.3498052.

[30] Wei Wang et al. “Beamforming Phased-Array-Fed Lenses With >0.5λ-Spaced Elements”. In: *IEEE Transactions on Antennas and Propagation* 3 (2023). DOI: 10.1109/TAP.2023.3240085.

[31] Michael Cooley. “Phased Array Fed Reflector (PAFR) antenna architectures for space-based sensors”. In: *2015 IEEE Aerospace Conference*. 2015. DOI: 10.1109/AERO.2015.7118963.

[32] Rogers Corporation. *A Gradient Index Lens to Enable 180-Degree Field-of-View in a Phased Array System*. Microwave Journal. 2022. URL: https://www.microwavejournal.com/articles/37786-a-gradient-index-lens-to-enable-180-degree-field-of-view-in-a-phased-array-system.

[33] V. Judin et al. “Design of a Field-of-View Enhancing Lens for mmWave 5G Radios Using Gradient Index Approach”. In: *2024 IEEE International Symposium on Antennas and Propagation and INC/USNC□URSI Radio Science Meeting (AP-S/INC-USNC-URSI)*. 2024. DOI: 10.1109/AP-S/INC-USNC-URSI52054.2024.10686087.

[34] J. C. Maxwell Garnett. “XII. Colours in metal glasses and in metallic films”. In: *Philosophical Transactions of the Royal Society of London, Series A: Containing Papers of a Mathematical or Physical Character* 359-371 (1904). DOI: 10.1098/rsta.1904.0024.

[35] Simon P. Hehenberger, Stefano Caizzone, Stefan Thurner, and Alexander G. Yarovoy. “Broadband Effective Permittivity Simulation and Measurement Techniques for 3-D-Printed Dielectric Crystals”. In: *IEEE Transactions on Microwave Theory and Techniques* 10 (2023). DOI: 10.1109/TMTT.2023.3259479.

[36] Simon P. Hehenberger, Stefano Caizzone, and Alexander Yarovoy. “Modeling and measurement of dielectric anisotropy in materials manufactured via fused filament fabrication processes”. In: *Materials Research Bulletin* (2024). DOI: 10.1016/j.materresbull.2024.112938.

[37] Noel P. Martinez et al. “Spatially-Variant Photonic Crystals and Possible Applications”. In: *2018 IEEE Research and Applications of Photonics In Defense Conference (RAPID)*. 2018. DOI: 10.1109/RAPID.2018.8509003.

[38] J. E. Santos, R. B. Ruben, P. R. Fernandes, and A. P. G. Castro. “LISBON TPMS TOOL: An open-source tool for the design of TPMS structures for engineering applications”. In: *Software Impacts* (2025). DOI: 10.1016/j.simpa.2025.100747.

[39] Mahtab Vafaeefar and Kevin Mattheus Moerman. *LatticeWorks*. 2024. DOI: 10.5281/zenodo.13862475.

[40] Nanoe. *Zetamix Epsilon Datasheet*. 6 rue des frênes, 91160 Ballainvilliers, France: Nanoe, 2024.

[41] Mateusz M. Krysicki, Bartlomiej W. Salski, Tomasz Karpisz, and Pawel Kopyt. “Complex Permittivity of 3D-Printing Filaments in the 20 - 50 GHz Frequency Band”. In: *2021 51st European Microwave Conference (EuMC)*. 2022. DOI: 10.23919/EuMC50147.2022.9784173.

[42] David B. Davidson. *Computational Electromagnetics for RF and Microwave Engineering*. 2nd ed. Cambridge: Cambridge University Press, 2010. ISBN: 978-0-521-51891-8. DOI: 10.1017/CBO9780511778117.

[43] Leonard Besse, Yanki Aslan, Sourav Patranabish, and Kunal Masania. “Fourier Series–Based Optimization of Gradient Index Lens Permittivity Profiles Within Manufacturing Limits”. In: *2026 20th European Conference on Antennas and Propagation (EuCAP)*. 2026.

[44] Wei Wang, Philip Lambert, and Jonathan Chisum. “High-Frequency Limits for 3D-Printed Gradient-Index (GRIN) Lens Antennas”. In: *2023 IEEE International Symposium on Antennas and Propagation and USNC-URSI Radio Science Meeting (USNC-URSI)*. 2023. DOI: 10.1109/USNC-URSI52151.2023.10237634.

[45] Miguel Fernandez-Vicente, Wilson Calle, Santiago Ferrandiz, and Andres Conejero. “Effect of Infill Parameters on Tensile Mechanical Behavior in Desktop 3D Printing”. In: *3D Printing and Additive Manufacturing* 3 (2016). DOI: 10.1089/3dp.2015.0036.

[46] Kuek Chee Yaw. *Measurement of Dielectric Material Properties*. Application Note. Rohde & Schwarz, 2012.

[47] Max Born and Emil Wolf. *Principles of Optics: Electromagnetic Theory of Propagation, Interference and Diffraction of Light*. 7th ed. Cambridge: Cambridge University Press, 1999. DOI: 10.1017/CBO9781139644181.

A

Mathematical Conventions

In this work, vectors are generally indicated in bold:

$$\mathbf{k} = \begin{bmatrix} k_x \\ k_y \\ k_z \end{bmatrix}$$

An exception is made for unit vectors. These are indicated with a hat;

$$|\hat{s}| = 1$$

We take a counter-clockwise rotation for phasors, following the electrical engineering convention. On the same note, we use the notation $j = \sqrt{-1}$.

$$\mathbf{E} = \mathrm{Re}(\mathbf{E}_0 e^{j(\omega t - \mathbf{k}\cdot\mathbf{r})})$$

The coordinate system below is used when parametrizing the GRIN lens, also shown in Figure 2.9.

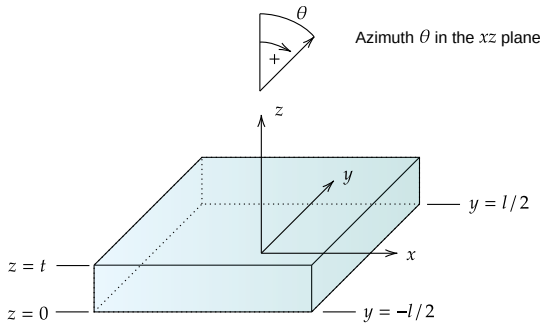

Figure A.1: Coordinate system used in this work.

B

Derivation of Ray Optics

This derivation shown here closely follows the one found in chapter 3 of Born and Wolf's Principle of Optics [47]. We begin with Maxwell's equations in phasor form without sources;

$$\nabla \times \mathbf{E} = -j\omega\mu\mathbf{H} \tag{B.1}$$
$$\nabla \times \mathbf{H} = j\omega\varepsilon\mathbf{E} \tag{B.2}$$
$$\nabla \cdot \varepsilon\mathbf{E} = 0 \tag{B.3}$$
$$\nabla \cdot \mu\mathbf{H} = 0 \tag{B.4}$$

An electromagnetic wave far away from the sources can be described generally as

$$\mathbf{E}(\mathbf{r}) = \mathbf{E}_0(\mathbf{r})e^{-jk_0\psi(\mathbf{r})} \tag{B.5}$$
$$\mathbf{H}(\mathbf{r}) = \mathbf{H}_0(\mathbf{r})e^{-jk_0\psi(\mathbf{r})} \tag{B.6}$$

where $\psi(\mathbf{r})$ is a scalar function representing optical distance, and $\psi(\mathbf{r}) =$ *constant* describes a geometrical wavefront.

We substitute Equation B.5 and Equation B.6 into Equation B.1;

$$\nabla \times \mathbf{E} = -j\omega\mu\mathbf{H}$$
$$\nabla \times (\mathbf{E}_0 e^{-jk_0\psi}) = -j\omega\mu\mathbf{H}_0 e^{-jk_0\psi}$$

Then, using the vector calculus identity $\nabla \times (\varphi\mathbf{A}) = \nabla\varphi \times \mathbf{A} + \varphi\nabla \times \mathbf{A}$;

$$\nabla e^{-jk_0\psi} \times \mathbf{E}_0 + e^{-jk_0\psi}\nabla \times \mathbf{E}_0 = -j\omega\mu\mathbf{H}_0 e^{-jk_0\psi}$$
$$-jk_0 e^{-jk_0\psi}\nabla\psi \times \mathbf{E}_0 + e^{-jk_0\psi}\nabla \times \mathbf{E}_0 = -j\omega\mu\mathbf{H}_0 e^{-jk_0\psi}$$

Dividing by $-jk_0e^{-jk_0\psi}$;

$$\nabla\psi \times \mathbf{E}_0 + \frac{1}{-jk_0}\nabla \times \mathbf{E}_0 = \mu\frac{\omega}{k_0}\mathbf{H_0}$$

Since ω/k_0 is the speed of light c_0, we then have

$$\boxed{\nabla\psi \times \mathbf{E}_0 - \mu c_0\mathbf{H_0} = \frac{1}{jk_0}\nabla \times \mathbf{E}_0}$$

We now substitute Equation B.5 into Equation B.3;

$$\nabla \cdot \varepsilon(\mathbf{E}_0e^{-jk_0\psi}) = 0$$

Using the identity $\nabla \cdot (\psi\varphi\mathbf{A}) = (\varphi\nabla\psi + \psi\nabla\varphi) \cdot \mathbf{A} + \varphi\psi\nabla \cdot \mathbf{A}$;

$$\begin{aligned}\left(\varepsilon\nabla e^{-jk_0\psi} + e^{-jk_0\psi}\nabla\varepsilon\right) \cdot \mathbf{E}_0 + \varepsilon e^{-jk_0\psi}\nabla \cdot \mathbf{E}_0 = 0\\ -\varepsilon jk_0e^{-jk_0\psi}\nabla\psi \cdot \mathbf{E}_0 + e^{-jk_0\psi}\nabla\varepsilon \cdot \mathbf{E}_0 + \varepsilon e^{-jk_0\psi}\nabla \cdot \mathbf{E}_0 = 0\end{aligned}$$

Dividing by $-jk_0\varepsilon e^{-jk_0\psi}$, we have

$$\nabla\psi \cdot \mathbf{E}_0 = \frac{-\mathbf{E}_0 \cdot \nabla\varepsilon - \varepsilon\nabla \cdot \mathbf{E}_0}{-jk_0\varepsilon}$$

With $\frac{1}{\varepsilon}\nabla\varepsilon = \nabla \ln\varepsilon$, we finally have

$$\boxed{\nabla\psi \cdot \mathbf{E}_0 = \frac{1}{jk_0}\left(\mathbf{E}_0 \cdot \nabla \ln\varepsilon + \nabla \cdot \mathbf{E}_0\right)}$$

Repeating the above with Equation B.2 and Equation B.4, we obtain the following equations

$$\nabla\psi \times \mathbf{H}_0 + \varepsilon c_0\mathbf{E}_0 = \frac{1}{jk_0}\nabla \times \mathbf{H}_0 \tag{B.7}$$

$$\nabla\psi \times \mathbf{E}_0 - \mu c_0\mathbf{H}_0 = \frac{1}{jk_0}\nabla \times \mathbf{E}_0 \tag{B.8}$$

$$\nabla\psi \cdot \mathbf{E}_0 = \frac{1}{jk_0}\left(\mathbf{E}_0 \cdot \nabla \ln\varepsilon + \nabla \cdot \mathbf{E}_0\right) \tag{B.9}$$

$$\nabla\psi \cdot \mathbf{H}_0 = \frac{1}{jk_0}\left(\mathbf{H}_0 \cdot \nabla \ln\mu + \nabla \cdot \mathbf{H}_0\right) \tag{B.10}$$

The key assumption of geometrical optics is that the wavelength is very small[1]. Equivalently, since $k_0 = 2\pi/\lambda_0$, we have $k_0 \to \infty$. The equations above then simplify to

$$\nabla\psi \times \mathbf{H}_0 = -\varepsilon c_0 \mathbf{E}_0 \tag{B.11}$$
$$\nabla\psi \times \mathbf{E}_0 = \mu c_0 \mathbf{H}_0 \tag{B.12}$$
$$\nabla\psi \cdot \mathbf{E}_0 = 0 \tag{B.13}$$
$$\nabla\psi \cdot \mathbf{H}_0 = 0 \tag{B.14}$$

As a brief aside, we can make a more precise statement about the GO assumption. Specifically, we see that the following should hold;

$$k_0 \gg \mathbf{E}_0 \cdot \nabla \ln\varepsilon + \nabla \cdot \mathbf{E}_0$$

The $\nabla \ln\varepsilon$ term has an important implication for GRIN media; it implies that the spatial rate of change of the refractive index must be small compared to the wavelength.

Continuing with the derivation, we can then rearrange Equation B.11 and substitute it into Equation B.12;

$$\mathbf{E}_0 = \frac{1}{\varepsilon c_0}\nabla\psi \times \mathbf{H}_0$$
$$\nabla\psi \times \left(\frac{1}{\varepsilon c_0}\nabla\psi \times \mathbf{H}_0\right) = \mu c_0 \mathbf{H}_0$$

Then, using the identity $\mathbf{a} \times (\mathbf{b} \times \mathbf{c}) = (\mathbf{a}\cdot\mathbf{c})\mathbf{b} - (\mathbf{a}\cdot\mathbf{c})\mathbf{b}$, we obtain

$$\frac{1}{\varepsilon c_0}\left((\nabla\psi \cdot (\mathbf{H}_0)\nabla\psi - (\nabla\psi)^2\mathbf{H}_0\right) = \mu c_0 \mathbf{H}_0$$

Substituting Equation B.14 and factoring out $\mathbf{H}_0$, this simplifies to

$$\frac{1}{\varepsilon c_0}\left(-(\nabla\psi)^2\mathbf{H}_0\right) = \mu c_0 \mathbf{H}_0$$
$$(\nabla\psi)^2 = \varepsilon\mu c_0^2$$

Since $\varepsilon\mu = \varepsilon_0\varepsilon_r\mu_0\mu_r = (\sqrt{\varepsilon_r\mu_r})^2(\sqrt{\varepsilon_0\mu_0})^2 = n^2/c_0^2$, we finally obtain

$$\boxed{(\nabla\psi)^2 = n^2} \tag{B.15}$$

[1] Born and Wolf describe this as 'a complete neglect of the finiteness of the wavelength' [47].

Equation B.15 is known as the *eikonal equation*, and is one of the key equations in the study of optics (it should be noted that ψ is often simply referred to as the eikonal). From the eikonal equation, we can write Equation B.16.

$$|\nabla\psi| = n \tag{B.16}$$

From here, we can also derive the equation for light rays, for use in Equation 2.5. The wave travels perpendicular to the wavefront, in the direction of the Poynting vector $\mathbf{S}$;

$$\mathbf{S} = \frac{1}{2}\mathbf{E_0} \times \mathbf{H}_0^*$$

Once again using Equation B.12 and the identity for the cross product of a cross product, we have

$$\mathbf{S} = \frac{1}{2}\left(\mathbf{E}_0 \times \frac{1}{\mu c_0}\left(\nabla\psi \times \mathbf{E}_0^*\right)\right) = \frac{1}{2\mu c_0}\left(\mathbf{E}_0 \times \nabla\psi \times \mathbf{E}_0^*\right)$$
$$\mathbf{S} = \frac{1}{2\mu c_0}\left(|\mathbf{E}_0|^2\nabla\psi - \left(\nabla\psi \cdot \mathbf{E}_0\right)\mathbf{E}_0^*\right)$$

With Equation B.13, this simplifies to

$$\mathbf{S} = \frac{|\mathbf{E}_0|^2}{2\mu c_0}\nabla\psi \tag{B.17}$$

From Equation B.17, we see that the Pyonting vector is in the direction of $\nabla\psi$. We can then define the unit vector $\hat{s}$.

$$\hat{s} = \frac{\nabla\psi}{|\nabla\psi|} = \frac{\nabla\psi}{n} \tag{B.18}$$

Consider now the position a point on a ray $\mathbf{r}(s)$, where s is the arc length along the ray. If we advance along the ray to the position by a small distance ds, the resulting vector $\mathbf{r}(s+ds) - \mathbf{r}(s) = \hat{s}ds$. Or, in differential form,

$$\frac{d\mathbf{r}(s)}{ds} = \hat{s}$$

Using Equation B.18, we can rewrite this as

$$n\frac{d\mathbf{r}(s)}{ds} = \nabla\psi \tag{B.19}$$

We can then take the derivative of Equation B.19 with respect to s, using the identities $\nabla((\nabla\psi)^2) = 2\nabla\psi \cdot \nabla(\nabla\psi)$ and $\nabla n^2 = 2n\nabla n$.

$$\begin{aligned}
\frac{d}{ds}\left(n\frac{d\mathbf{r}(s)}{ds}\right) &= \frac{d}{ds}(\nabla\psi) \\
&= \frac{d\mathbf{r}(s)}{ds}\nabla(\nabla\psi) \\
&= \frac{1}{n}\nabla\psi\nabla(\nabla\psi) && \text{(From Equation B.19)} \\
&= \frac{1}{2n}\nabla((\nabla\psi)^2) \\
&= \frac{1}{2n}\nabla n^2 && \text{(From Equation B.15)}
\end{aligned}$$

Therefore,

$$\frac{d}{ds}\left(n\frac{d\mathbf{r}}{ds}\right) = \nabla n \tag{B.20}$$

As was done by Gashi in [9], it is convenient to use the optical length t (i.e. the arc length along the ray multiplied by the refractive index at that point, $dt = nds$). This allows us to directly compute the phase $\phi = k_0 t$.

From this, we finally arrive to Equation 2.5, which is then solved numerically.

$$\begin{aligned}
y(t) &= \begin{bmatrix} \mathbf{r}(t) \\ \nabla\psi(t) \end{bmatrix} \\
y'(t) &= \begin{bmatrix} \mathbf{r}'(t) \\ \nabla\psi'(t) \end{bmatrix} = \begin{bmatrix} \nabla\psi(t)/n^2 \\ \nabla n/n \end{bmatrix}
\end{aligned}$$

C

On the Phase Model ϕ_{target}

Here, we motivate Equation 2.21, in particular for the relation shown in Equation C.1. The steps shown here are very loosely based on the derivation of the array factor in section 6.6 of Balanis [2].

$$\phi_{target} = k_0(\hat{u}_{target} \cdot \mathbf{r}_{ap}) \tag{C.1}$$

We consider first a flat aperture with a target in the far field. Consider the aperture in reception; looking at Figure C.1, we see that the point at $\mathbf{r}_{ap}$ is slightly ahead of the origin, by a distance of d.To convert this distance to radians, we have

$$\phi = \frac{2\pi}{\lambda_0} d = k_0 d \tag{C.2}$$

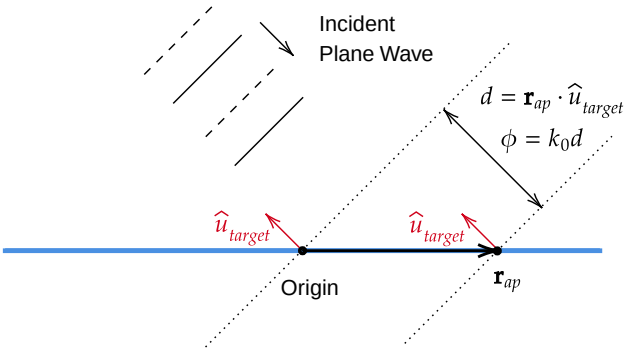

Figure C.1: Illustration of the phase model for a flat aperture with an incident plane wave.

One must be careful with the chosen sign convention; here, a negative value of ϕ indicates a phase delay, with the phasor convention defined in Appendix A. Looking at the aperture in transmission, we see that the sources at the origin must be delayed compared to $\mathbf{r_{ap}}$.

It is perhaps not immediately obvious that this model can be applied to the flat lens designed in this thesis. To motivate this, we consider two rays close to each other. With the matrix $[T]$ described by Equation 2.18, we see that $\hat{u}_{target}$ should be similar for each ray, as shown in Figure C.2.

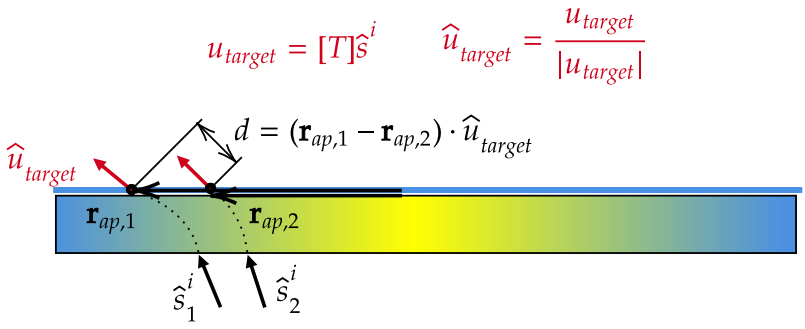

Figure C.2: Illustration of the phase model on a flat GRIN lens.

A precise derivation is unfortunately out of the reach of this author. Nevertheless, as this phase model is a critical element of the work presented here, we further motivate it by showing that this is equivalent to the phase model used by Budhu et al. in [17]. There, the authors used

$$\phi_{target} = k_0 \sin(\theta_b)\cos(\varphi_b)x_{ap} + k_0 \sin(\theta_b)\sin(\varphi_b)y_{ap} \tag{C.3}$$

Where θ_b and φ_b are the spherical angles for the intended beam peak. Converting to a vector, the unit vector $\hat{u}_{target}$ is given by

$$\hat{u}_{target} = \begin{bmatrix} \sin(\theta_b)\cos(\varphi_b) \\ \sin(\theta_b)\sin(\varphi_b) \\ \cos(\theta_b) \end{bmatrix} \tag{C.4}$$

The coordinates x_{ap} and y_{ap} in Equation C.3 refer to the position on a flat aperture. We can then clearly see that the proposed phase model is equivalent to Equation C.3;

$$\phi_{target} = k_0(\hat{u}_{target} \cdot \mathbf{r}_{ap}) = \begin{bmatrix} \sin(\theta_b)\cos(\varphi_b) \\ \sin(\theta_b)\sin(\varphi_b) \\ \cos(\theta_b) \end{bmatrix} \cdot \begin{bmatrix} x_{ap} \\ y_{ap} \\ 0 \end{bmatrix} = k_0 \sin(\theta_b)\cos(\varphi_b)x_{ap} + k_0 \sin(\theta_b)\sin(\varphi_b)y_{ap} \tag{C.5}$$